

# 1 Extended Magnetohydrodynamics with Embedded 2 Particle-in-Cell Simulation of Ganymede's 3 Magnetosphere

Gábor Tóth<sup>1</sup>, Xianzhe Jia<sup>1</sup>, Stefano Markidis<sup>3</sup>, Ivy Bo Peng<sup>3</sup>, Yuxi Chen<sup>1</sup>,  
Lars K.S. Daldorff<sup>2</sup>, Valeriy M. Tenishev<sup>1</sup>, Dmitry Borovikov<sup>1</sup>, John D.  
Haiducek<sup>1</sup>, Tamas I. Gombosi<sup>1</sup>, Alex Gloer<sup>2</sup>, John C. Dorelli<sup>2</sup>

- 4 First particle-in-cell simulation of Ganymede's magnetosphere.
- 5 The MHD-EPIC algorithm makes global kinetic simulations affordable.
- 6 MHD-EPIC simulation suggests that Galileo observed a flux transfer event during the G8 flyby.

---

G. Toth, Univ. of Michigan, 2455 Hayward, Ann Arbor, MI 48109 (gtoth@umich.edu)

<sup>1</sup> Center for Space Environment

Modeling, University of Michigan, Ann  
Arbor, MI, USA.

<sup>2</sup> NASA Goddard Space Flight Center,  
Greenbelt, MD, USA.

<sup>3</sup> KTH, Stockholm, Sweden.

This is the author manuscript accepted for publication and has undergone full peer review but has not been through the copyediting, typesetting, pagination and proofreading process, which may lead to differences between this version and the Version of Record. Please cite this article as doi:

10.1029/2015JA021997

January 21, 2016, 3:53am

D R A F T

**Abstract.** We have recently developed a new modeling capability to embed the implicit Particle-in-Cell (PIC) model iPIC3D into the BATS-R-US magnetohydrodynamic (MHD) model. The MHD with Embedded PIC domains (MHD-EPIC) algorithm is a two-way coupled kinetic-fluid model. As one of the very first applications of the MHD-EPIC algorithm, we simulate the interaction between Jupiter's magnetospheric plasma and Ganymede's magnetosphere. We compare the MHD-EPIC simulations with pure Hall MHD simulations and compare both model results with Galileo observations to assess the importance of kinetic effects in controlling the configuration and dynamics of Ganymede's magnetosphere. We find that the Hall MHD and MHD-EPIC solutions are qualitatively similar, but there are significant quantitative differences. In particular, the density and pressure inside the magnetosphere show different distributions. For our baseline grid resolution the PIC solution is more dynamic than the Hall MHD simulation and it compares significantly better with the Galileo magnetic measurements than the Hall MHD solution. The power spectra of the observed and simulated magnetic field fluctuations agree extremely well for the MHD-EPIC model. The MHD-EPIC simulation also produced a few flux transfer events (FTEs) that have magnetic signatures very similar to an observed event. The simulation shows that the FTEs often exhibit complex 3D structures with their orientations changing substantially between the equatorial plane and the Galileo trajectory, which explains the magnetic signatures observed during the magnetopause

29 crossings. The computational cost of the MHD-EPIC simulation was only  
30 about 4 times more than that of the Hall MHD simulation.

Author Manuscript

## 1. Introduction

31 Ganymede's magnetosphere is unique in the solar system. The Jovian moon is or-  
 32 biting inside the Jovian magnetosphere but it has its own intrinsic field that forms a  
 33 small magnetosphere around Ganymede. The Jovian plasma flows at a subsonic and sub-  
 34 Alfvénic speed relative to Ganymede, so the moon's magnetosphere produces an Alfvén  
 35 wing [Neubauer, 1998] instead of a bow shock present around planetary magnetospheres.  
 36 Since the Jovian magnetic field is roughly anti-parallel with Ganymede's intrinsic magnetic  
 37 field at the magnetopause, the configuration of Ganymede's magnetosphere is analogous  
 38 with the interaction of Earth's magnetosphere with a southward pointing interplanetary  
 39 magnetic field (IMF). Therefore we expect reconnection concentrated at the upstream tip  
 40 of the magnetopause and in the magnetotail behind the moon.

41 The small size of Ganymede's magnetosphere provides a great opportunity to employ  
 42 our newly developed MagnetoHydroDynamics with Embedded Particle-In-Cell (MHD-  
 43 EPIC) model [Daldorff et al., 2014]. Ganymede interacts with the plasma co-rotating  
 44 with Jupiter that we refer to as the Jovian wind. The ion inertial length in the Jovian  
 45 wind with mass density  $\rho \approx 56 m_p/\text{cm}^{-3}$  consisting of a mixture of  $O^+$  and  $H^+$  ions  
 46 with an average mass  $M_i = 14 m_p$  is about  $0.16 R_G$  where  $m_p = 1.67 \times 10^{-27}$  kg is the  
 47 proton mass and  $R_G = 2,634$  km is Ganymede's radius. In comparison, the standoff  
 48 distance of the magnetopause is about  $2 R_G$ , and the tail reconnection is expected to  
 49 occur within about  $4 R_G$  [Kivelson et al., 1998; Jia et al., 2010; Jia, 2015]. Due to the  
 50 small electron mass  $M_e$ , the electron inertial length is much ( $\sqrt{M_i/M_e}$  times) smaller than  
 51 the ion inertial length. Kinetic simulations show, however, that the reconnection process

52 is not very sensitive to the electron mass as long as  $M_i/M_e \geq 100$  [*Ricci et al.*, 2002;  
53 *Lapenta et al.*, 2010]. This means that using an artificially increased electron mass of  
54  $M_e \sim M_i/100$  the particle-in-cell (PIC) code has a chance to capture even the electron  
55 scales.

56 Previous work on modeling Ganymede's magnetosphere in three dimensions (3D) in-  
57 clude resistive MHD [*Kopp and Ip*, 2002; *Jia et al.*, 2008, 2009, 2010; *Duling et al.*, 2014],  
58 Hall MHD [*Dorelli et al.*, 2015] and multi-fluid [*Paty and Winglee*, 2004; *Paty et al.*, 2008]  
59 simulations. We refer to *Dorelli et al.* [2015] for a more in-depth comparison among these  
60 models that all use a fluid description for the plasma. The reconnection physics in these  
61 magneto-fluid models relies on either Hall resistivity, or ad hoc anomalous resistivity, or  
62 simply numerical resistivity. In addition, the distribution function of the ions and elec-  
63 trons is assumed to be Maxwellian. Using a particle-in-cell model therefore can reveal the  
64 importance of the kinetic effects, as it captures the microscopic dissipation mechanisms  
65 that lead to reconnection based on first principles. Thanks to the Galileo observations  
66 [e.g. *Kivelson et al.*, 1997] the models can be compared not only with each-other, but also  
67 validated against in-situ measurements of magnetic field.

68 Although Ganymede's magnetosphere is small, the simulation domain has to be much  
69 larger to provide sufficient space for the Alfvén wings and the subsonic and sub-Alfvénic  
70 interaction with the Jovian wind. In fact, it is quite challenging to provide proper bound-  
71 ary conditions for subsonic/Alfvénic inflow and outflow. The best approach is to place  
72 the boundaries far enough so that Ganymede's effect on the plasma is negligible near the  
73 boundaries. We found it was necessary to make the simulation box about  $200 R_G$  wide  
74 in all three directions to make the effects of the boundaries truly insignificant. Doing a

75 pure PIC simulation in such a large domain while resolving at least the ion inertial length  
76 would be extremely demanding computationally.

77 Fortunately the new MHD-EPIC algorithm provides a feasible alternative: the large  
78 computational domain can be efficiently modeled with the Hall MHD code, while the  
79 vicinity of the moon, where kinetic effects are potentially important, is modeled with the  
80 PIC code. The Hall MHD and PIC models are two-way coupled to ensure the consistency  
81 of the solution. The MHD-EPIC algorithm can provide a global time-dependent solution  
82 where all the critical dynamics is handled by the PIC code. As we will show in this paper,  
83 the MHD-EPIC model provides a solution that is similar to but significantly different  
84 from the Hall MHD solution reported by *Dorelli et al.* [2015].

85 The computational models and the simulation set up are described in section 2, the  
86 main simulation results and comparison with measurements are presented in section 3,  
87 additional simulations are described in section 4, and we conclude with section 5.

## 2. Model Description

88 This paper presents the first three-dimensional (3D) application of the recently devel-  
89 oped Hall Magnetohydrodynamics with Embedded Particle-In-Cell (MHD-EPIC) model  
90 [*Daldorff et al.*, 2014]. The Hall MHD equations are solved by the BATS-R-US code  
91 [*Powell et al.*, 1999; *Tóth et al.*, 2008], while the embedded PIC regions are simulated by  
92 the iPIC3D code [*Markidis et al.*, 2010]. The two codes are coupled together in the Space  
93 Weather Modeling Framework (SWMF) [*Tóth et al.*, 2005, 2012]. This section describes  
94 the models and the coupling in some detail. We concentrate on the particular algorithms  
95 and settings used in the Ganymede simulations.

## 2.1. Hall Magnetohydrodynamic Model: BATS-R-US

Block-Adaptive-Tree-Solarwind-Roe-Upwind-Scheme (BATS-R-US) is a flexible global MHD code that has been extensively used to study plasma interactions with a variety of solar system bodies including planets, planetary moons, and comets. BATS-R-US allows adaptive mesh refinement in combination with curvilinear coordinates. For the simulations here, an adaptive Cartesian grid is employed in a  $-128 R_G < x, y, z < 128 R_G$  cube in the GphiO coordinates centered around Ganymede. The X axis points in the direction of the Jovian wind, the Z axis is parallel to the Jovian rotational axis, and the Y axis completes the coordinate system pointing approximately toward Jupiter. The smallest cell size is  $1/32 R_G$  in a box  $-3 R_G < x < 4 R_G$ ,  $-3 R_G < y < 3 R_G$  and  $-2 R_G < z < 2 R_G$  and gradually coarser further away up to  $4 R_G$  cells. The total number of BATS-R-US grid cells is about 8.5 million.

The moon is represented by a spherical inner boundary at radial distance  $1 R_G$ . We apply absorbing boundary conditions here: if the plasma velocity points toward the surface then a zero-gradient is applied, while if the velocity is pointing away from the surface, then the radial component of the velocity is reversed. The transverse components of the velocity, the density and the pressure always have zero gradients. The magnetic field  $\mathbf{B}$  is split into the intrinsic dipole field  $\mathbf{B}_0$  and the deviation  $\mathbf{B}_1$ . The  $\mathbf{B}_0$  field is calculated analytically from a magnetic dipole pointing approximately in the  $-Z$  direction with 719 nT field strength at the equator [Kivelson *et al.*, 2002]. The magnetic axis is tilted by  $4.37^\circ$  relative to the Z axis and it intersects the surface at  $289^\circ$  longitude on the northern hemisphere. The boundary condition is zero gradient for the transverse components of  $\mathbf{B}_1$

117 and reflective for the radial component of  $\mathbf{B}_1$ . These inner boundary conditions are crucial  
 118 for obtaining the correct size (that is consistent with Galileo data) for the magnetosphere.

119 In this paper, we focus on comparing our model results with Galileo observations ob-  
 120 tained during the G8 flyby that passed through the upstream magnetopause and thus  
 121 it is the most relevant for looking at kinetic effects. The G8 flyby took place when  
 122 Ganymede was located near the center of Jupiter's plasma sheet, so at the outer bound-  
 123 aries all the MHD quantities are fixed to the corresponding Jovian wind values following  
 124 *Jia et al.* [2008]: mass density  $\rho = 56 m_p/\text{cm}^{-3}$ , velocity  $u_x = 140 \text{ km/s}$ , magnetic field  
 125  $\mathbf{B} = (0, -6, -77) \text{ nT}$ , and total plasma pressure  $p = 3.8 \text{ nPa}$  from which the ion pressure  
 126 is  $p_i = 3.17 \text{ nPa}$  and the electron pressure is  $p_e = p_i/5 = 0.63 \text{ nPa}$ . The ion mass is taken  
 127 to be the average  $M_i = 14 m_p$ . Using fixed boundary conditions for all variables is an  
 128 overspecification from the mathematical point of view, but it works well numerically as  
 129 long as the outer boundaries are far enough from Ganymede. Simple fixed inflow and zero-  
 130 gradient outflow boundary conditions (typically used for the solar wind around planetary  
 131 magnetospheres) do not work for the subsonic and sub-Alfvénic Jovian wind.

132 It is important to check if the grid resolution is sufficiently fine to correctly repre-  
 133 sent the modeled physics. The ion inertial length in the Jovian wind is  $d_i = c/\omega_{pi} =$   
 134  $c/(1320\sqrt{n/M_i})$ , where  $c$  is the speed of light,  $n = 4$  is the number density in  $\text{cm}^{-3}$  units  
 135 and  $M_i = 14$  is the ion mass in proton mass. We get  $d_i \sim 425 \text{ km} \sim 0.16 R_G$  that is  
 136 resolved by about 5 to 6 grid cells of size  $\Delta x = 1/32 R_G = 82.3 \text{ km}$ . Another way to  
 137 see if the Hall term  $\mathbf{B} \times \mathbf{J}/(ne)$  matters in the induction equation is to compare the  
 138 maximum value of the Hall velocity  $u_H = \mathbf{J}/(ne)$  with the typical bulk velocity of the  
 139 plasma, where  $e = 1.6 \times 10^{-19} \text{ C}$  is the elementary charge. Given the magnetic field



140 strength  $B \sim 100$  nT and grid resolution  $\Delta x = 1/32 R_G$ , the maximum current den-  
 141 sity is  $J \sim (1/\mu_0)B/\Delta x \sim 10^{-6} A/m^2$ , so the maximum value of the Hall velocity is  
 142  $u_H \sim 1500$  km/s, which greatly exceeds the bulk velocity.

143 In addition to the Hall term, the electron pressure gradient term  $\nabla p_e/(ne)$  is also  
 144 included in the generalized Ohm's law. In this paper the electron pressure is simply taken  
 145 to be a fixed fraction (1/5th) of the ion pressure in the BATS-R-US model. The main  
 146 significance of this particular choice is that the electron pressure is passed to the PIC  
 147 code at the boundaries of the PIC region and we wish to keep the electron thermal speed  
 148 comparable to the ion thermal speed in the PIC code given the  $M_e \sim M_i/100$  choice for  
 149 the electron mass. This matters, because the implicit PIC time step is limited by the  
 150 electron thermal velocity divided by the cell size. While setting the electron pressure this  
 151 way is somewhat arbitrary, in essence it states that the plasma pressure is dominated by  
 152 the ions, which is not inconsistent with the plasma observations [Kivelson *et al.*, 2004].  
 153 In future work we will solve the electron pressure equation in the MHD code instead of  
 154 using a fixed fraction.

155 To speed up the BATS-R-US calculation, the Hall effect is restricted to the  $|x| < 4 R_G$ ,  
 156  $|y| < 3 R_G$ ,  $|z| < 2 R_G$  box centered around the moon. Outside this region the ideal MHD  
 157 equations are solved, which is a good approximation, since the currents are weak far from  
 158 the moon, so the Hall velocity  $u_H$  is very small.

159 The time discretization employs the explicit-implicit time stepping scheme [Tóth *et al.*,  
 160 2006] with a fixed time step  $\Delta t = 0.025$  s. The spatial discretization is based on the  
 161 second order accurate Rusanov scheme with Koren's 3rd order limiter. To further reduce  
 162 numerical diffusion while maintaining good convergence for the implicit solver, only 10%

163 of the whistler wave speed is taken into account for the maximum wave speed that is used  
 164 in the numerical flux of the Rusanov scheme [Tóth *et al.*, 2008]. The numerical divergence  
 165 of the magnetic field is controlled with the 8-wave scheme [Powell, 1994]. In some cases we  
 166 found that an additional hyperbolic cleaning [Dedner *et al.*, 2003] improves the magnetic  
 167 field solution across the MHD-PIC interface.

## 2.2. Implicit Particle-in-Cell Model: iPIC3D

168 In the embedded kinetic regions the solution is obtained by the implicit Particle-in-Cell  
 169 code iPIC3D [Markidis *et al.*, 2010]. iPIC3D solves the full set of Maxwell's equations for  
 170 the electromagnetic fields, coupled with the equations of motion for electrons and ions on  
 171 uniform 3D Cartesian grids. In the Ganymede simulations the cell size is  $\Delta x = 1/32 R_G \sim$   
 172 82.3 km in all PIC regions and the time step  $\Delta t = 0.025$  s is the same as for BATS-R-US.  
 173 The implicit PIC method is accurate as long as  $\Delta x/\Delta t \sim 3300$  km/s is larger than the  
 174 electron thermal speed, which is satisfied in the simulations. We note that, unlike explicit  
 175 PIC, the implicit PIC method remains stable against the finite grid instability even if the  
 176 grid does not resolve the Debye length.

177 Initially there are  $N_i = 216$  ion and  $N_e = 216$  electron macroparticles per grid cell.  
 178 As the simulation progresses, the particles can freely move in the PIC regions. When  
 179 a particle goes through the boundary, it is simply lost. On the other hand, the ghost  
 180 cells surrounding the PIC regions are filled in with  $N_i$  ions and  $N_e$  electrons every time  
 181 step, and these particles can move into the domain. The total number of particles can  
 182 vary somewhat during the run, but it typically remains close to the original number.  
 183 The ratio of ion and electron particle masses is set to  $M_i/M_e = 100$ , which is sufficiently  
 184 large to produce realistic reconnection dynamics. This means that the electron skin depth

185  $d_e = d_i/\sqrt{M_i/M_e} \sim 0.018 R_G$ , which is about half of the cell size  $\Delta x$ . Figure 1 shows the  
 186 X components of the ion and electron bulk velocities on the  $y=0$  plane inside the tail PIC  
 187 region. The electron jets emanating from the X-line of the reconnection are reasonably  
 188 well resolved as shown by the red and magenta regions in the bottom panel. Note that  
 189 the electron velocity is much larger than the ion velocity. The figure suggests that while  
 190 details at the electron scale are probably not accurate, the overall reconnection dynamics  
 191 should still be well captured.

### 2.3. MHD-EPIC Coupling within the Space Weather Modeling Framework

192 The BATS-R-US and iPIC3D models have been integrated into and coupled through  
 193 the Space Weather Modeling Framework (SWMF). Both models are compiled into a single  
 194 executable and they are initialized, advanced and coupled under the control of the SWMF.  
 195 Both models are massively parallel. In the Ganymede runs, BATS-R-US and all instances  
 196 of iPIC3D use all 960 CPU cores that the simulations were run with.

197 The MHD-EPIC algorithm has been described in detail by *Daldorff et al.* [2014]. Here  
 198 we describe the main idea and the new features and developments. First we obtain an  
 199 approximate steady state solution by running BATS-R-US in local time step mode (each  
 200 grid cell is advanced with the locally stable time step) for 100,000 time steps in the full  
 201 computational domain (see Figure 2). Then we restart the SWMF and specify the location  
 202 of the PIC regions.

203 At the beginning of the first time step of the restarted run, BATS-R-US sends the  
 204 MHD solution inside and around the PIC regions to iPIC3D, and iPIC3D initializes the  
 205 ion and electron macro particles with Maxwellian distributions that have the same mass,  
 206 momentum, and energy density as the MHD solution. From charge neutrality the number

207 densities of the electrons and ions are taken to be equal and obtained from the MHD  
 208 mass density  $\rho$  as  $n_i = n_e = \rho / (M_i + M_e)$ . The ion and electron velocities  $\mathbf{u}_i$  and  $\mathbf{u}_e$   
 209 are obtained from the following equations: 1) the total momentum  $M_i n_i \mathbf{u}_i + M_e n_e \mathbf{u}_e$   
 210 equals the  $\rho \mathbf{u}$  momentum of the MHD state; and 2) the current density derived in the  
 211 MHD code as  $\mathbf{J} = (1/\mu_0) \nabla \times \mathbf{B}$  equals  $ne(\mathbf{u}_i - \mathbf{u}_e)$ . The ion and electron pressures are  
 212 obtained from the total MHD pressure  $p$ . Since in these simulations the MHD code does  
 213 not solve for electron pressure, we take  $p_e = 0.2p_i$  and require that  $p = p_e + p_i$ . The ion  
 214 and electron macroparticles are then generated in each PIC computational cell with the  
 215 algorithm detailed by *Daldorff et al.* [2014]. The magnetic field  $\mathbf{B}$  is simply taken from  
 216 the MHD solution by the PIC code and the electric field is calculated as  $\mathbf{E} = -\mathbf{u}_e \times \mathbf{B}$ ,  
 217 which properly includes the Hall effect.

218 In subsequent time steps BATS-R-US still sends the MHD solution to iPIC3D, but it  
 219 is only used to generate particles in the ghost cells surrounding the PIC regions. On  
 220 the other hand, iPIC3D calculates the MHD quantities (mass density, momentum and  
 221 pressure) inside the PIC regions and sends them together with the magnetic field to  
 222 BATS-R-US, so that the MHD solution can be overwritten by the PIC solution inside the  
 223 PIC regions.

224 To facilitate the Ganymede simulations (and future MHD-EPIC applications), we have  
 225 developed a new general coupler in the SWMF to perform an efficient parallel coupling  
 226 algorithm that uses direct Message Passing Interface (MPI) data transfer between the  
 227 BATS-R-US and iPIC3D processes. The new coupler works for arbitrary 2D and 3D  
 228 grids, and it does not require the BATS-R-US and iPIC3D grids to be aligned or have the  
 229 same grid resolution. The implementation now also allows multiple PIC regions. We have

230 also implemented a new *tight coupling* option into the SWMF, where the two models are  
 231 coupled every time step and the length of the possibly varying time step is determined by  
 232 the *master* component (in this case BATS-R-US) and it is sent to the *slave* component  
 233 (in this case iPIC3D) so that the two models take the same time step. The tight coupling  
 234 allows the two models to remain fully in sync, which makes the solution at the coupling  
 235 interface more accurate and robust.

236 In the MHD-EPIC simulations of Ganymede's magnetosphere we use four PIC regions  
 237 that surround Ganymede but still cover all the potential reconnection sites as shown in  
 238 Figure 3. This is necessary, because the current version of iPIC3D cannot handle internal  
 239 boundaries, so the PIC regions cannot intersect with the surface of the moon at  $r = 1 R_G$ .  
 240 In units of  $R_G$  the upstream PIC region is placed at  $x \in [-2.875, -1.125]$ ,  $|y| < 2.875$   
 241 and  $|z| < 2.34375$ . The tail region is at  $x \in [1.125, 3.875]$ ,  $|y| < 2.875$  and  $|z| < 0.9375$ .  
 242 Finally the two flank regions are at  $|x| < 1.25$ ,  $y \in [\pm 1.125, \pm 2.875]$  and  $|z| < 1.875$   
 243 corresponding to the plus and minus signs, respectively. Given the  $\Delta x = 1/32 R_G$  grid  
 244 resolution in iPIC3D, the four regions consist of  $56 \times 184 \times 150 \sim 1.5$  million (upstream),  
 245  $88 \times 184 \times 60 \sim 1$  million (tail) and twice  $80 \times 56 \times 120 \sim 0.5$  million (flanks) grid cells.  
 246 The approximately 3.6 million PIC cells are initially filled with 216 ion and 216 electron  
 247 macroparticles per cell, which results in about 1.55 billion particles in total.

248 Although the four PIC regions slightly overlap at  $x \in [\pm 1.125, \pm 1.25]$ , currently there is  
 249 no direct communication among the PIC regions, so all information is going through the  
 250 MHD-EPIC coupling. This means that the distribution functions are set to be Maxwellian  
 251 at these boundaries just like at the other boundaries of the PIC regions. Since the main  
 252 reconnection sites are fully covered by the upstream and tail regions, the lack of direct

253 coupling between the PIC regions does not have a significant influence on the overall  
254 solution.

### 3. Results

255 We ran two simulations starting from the quasi-steady state solution obtained with the  
256 Hall MHD code. The first simulation simply continued the run with Hall MHD in time  
257 accurate mode, while the second simulation employed the Hall MHD-EPIC model with  
258 the four embedded PIC regions. Both simulations were continued for 10 minutes of phys-  
259 ical time, which is sufficient for the small magnetosphere to evolve into a quasi-periodic  
260 dynamics. The simulations could be run longer if needed, and we in fact performed longer  
261 runs up to 20 minutes. The simulations do not exhibit accumulation of numerical errors:  
262 the total mass, momentum and energy do not change significantly during the runs.

#### 3.1. Comparison of Hall MHD and Hall MHD-EPIC simulations

263 Figure 4 shows the Hall MHD and the Hall MHD-EPIC solutions at time  $t = 350$  sec-  
264 onds. The white lines are traces of the  $B_x$  and  $B_z$  components of the magnetic field, while  
265 the colors show the out-of-plane  $B_y$  component. The figure confirms that the reconnection  
266 sites are fully inside the upstream and tail-side PIC regions shown by the black rectangles  
267 in the right panel. This means that the reconnection is fully modeled by iPIC3D in the  
268 MHD-EPIC simulation. The solution goes smoothly through the boundaries of the PIC  
269 regions thanks to the two-way coupling with the MHD-EPIC algorithm.

270 The two solutions are clearly similar in terms of the overall configuration of the magne-  
271 tosphere, but there are also significant differences. Both models show the field signature  
272 typical of Hall reconnection near the upstream and tail reconnection sites. On the up-

273 stream side the PIC solution (right panel) shows a wider area with  $|B_y| > 50$  nT than the  
274 Hall MHD result (left panel). We confirmed that this difference does not disappear even  
275 if both models are run with twice finer grid resolution.

276 The PIC solution produces many flux transfer events (FTEs) at the upstream magne-  
277 topause during the 10 minute simulation as shown in the the movie provided in the online  
278 material. This quasi-periodic FTE production is similar to that obtained by *Jia et al.*  
279 [2010] using anomalous resistive MHD simulations. One of these events near the nose of  
280 the magnetopause is captured in the right panel of Figure 4. Interestingly, the Hall MHD  
281 simulation is much less dynamic, as it only produces very small islands at the dayside  
282 reconnection site. We note, however, that the FTE formation in the Hall MHD solution  
283 strongly depends on the grid resolution (this will be discussed in section 4). Figure 5  
284 shows the current density and velocity streamlines in the equatorial frame in a similar  
285 format as Figure 2 in [*Dorelli et al.*, 2015], although the coordinate systems are flipped.  
286 Both simulations show a pronounced asymmetry with respect to the  $\pm Y$  direction similar  
287 to that found by *Dorelli et al.* [2015] in their Hall MHD simulations but not in their  
288 resistive MHD solution. This confirms that the asymmetry is a consequence of the Hall  
289 physics that is captured by both the Hall MHD and the kinetic PIC simulations. The  
290 Hall MHD solution shows clear signatures of the Kelvin-Helmholtz (KH) instability in  
291 the  $-X, +Y$  quadrant of the magnetopause. The PIC solution also has small ripples in  
292 the same part of the magnetopause, but the wavelength and the amplitude are smaller  
293 than in the Hall MHD solution. It is likely that the difference is due to kinetic effects,  
294 such as finite Larmor radius, not captured by the Hall MHD scheme. We note that KH  
295 observations at Mercury show similar dawn-dusk asymmetry [*Liljeblad et al.*, 2014].

296 Although the magnetic field structures of the two simulations look quite similar, some  
297 of the plasma parameters, such as density and pressure, are quite different. Figures 6  
298 and 7 show the density and pressure in the meridional and equatorial cut planes. Inside  
299 the magnetosphere, especially on the tail side, the density is much smaller in the Hall  
300 MHD simulation than in the MHD-EPIC simulation. The MHD-EPIC solution shows a  
301 density peak with  $\rho > 70 \text{ amu/cm}^3$  on the moon side of the tail reconnection. The Hall  
302 MHD solution does not have a similar feature. In the MHD-EPIC simulation the pressure  
303 is reduced in the closed field line region on the upstream side and increased on the tail  
304 side compared to the Hall MHD simulation. The MHD-EPIC pressure shows a similar  
305 enhancement as the density on the tail side. This is likely a result of the reconnection  
306 jet hitting the closed field lines. The Hall MHD pressure is also enhanced slightly, but  
307 with much smaller values. These comparisons show that Hall MHD and PIC produce  
308 significantly different solutions in the regions affected by the magnetic reconnection. These  
309 differences are not sensitive to grid resolution (see section 4).

### 3.2. Comparison with Galileo magnetic field measurements

310 While comparing the Hall MHD and PIC solutions provides insight into the importance  
311 of kinetic effects, it is even more important to make sure that the simulations are consis-  
312 tent with measurements. This section compares the simulations with the magnetic data  
313 obtained during the Galileo G8 flyby on May 7, 1997. Figure 8 compares measured (black  
314 line) and simulated (blue line) magnetic fields extracted from the MHD-EPIC simulation  
315 at an arbitrary fixed simulation time ( $t = 99 \text{ s}$ ). The observation time on the horizontal  
316 axis is measured in minutes relative to 00 UT of May 7, 1997. Clearly, there is a dis-  
317 crepancy, especially in the  $B_x$  component. The agreement can be improved substantially



318 if the data is extracted from a modified trajectory that is obtained by multiplying the  
 319 trajectory coordinates by 1.06. This corresponds to a radial stretching by 6%. The mag-  
 320 netic field extracted along the stretched trajectory is shown by the red line, which agrees  
 321 quite well with the observations. This means that the simulated magnetosphere is slightly  
 322 larger than it should be. This is most likely caused by the inner boundary conditions that  
 323 provide a rather crude representation of the electric resistivity of the moon. We note that  
 324 *Dorelli et al.* [2015] applied a similar adjustment (an outward offset by  $0.05 R_G$  in the  $x$   
 325 and  $z$  directions) to improve the agreement with observations.

326 The optimal stretching factor was determined by minimizing the difference between the  
 327 measured and simulated magnetic field components inside the magnetosphere (between  
 328 952 min and 962 min observation times). For the MHD-EPIC simulation the optimal  
 329 stretching factor is  $s = 1.06$  resulting in an average difference of  $|\Delta B_{xyz}| = 12.5$  nT. For  
 330 the Hall MHD simulation the optimal value is at  $s = 1.08$  with  $|\Delta B_{xyz}| = 14.7$  nT. For  
 331 sake of simplicity we use  $s = 1.06$  for both models noting that this results in a moderate  
 332 increase in  $|\Delta B_{xyz}|$  to 15.6 nT for the Hall MHD simulation.

333 We continue our data comparison by using the radially stretched (by 6%) trajectory and  
 334 concentrate on the shape of the magnetic signatures. Due to the dynamic and somewhat  
 335 chaotic nature of the reconnection process, one cannot hope to produce a point-to-point  
 336 match with Galileo observations. Our simulations cover 10 minute physical time, which  
 337 is long compared to the dynamic time scales, but shorter than the duration of the flyby:  
 338 Galileo measured clear magnetic signatures due to Ganymede's magnetosphere for about  
 339 15-20 minutes. To make a meaningful comparison with Galileo, we have stacked the  
 340 simulations repeatedly to cover the whole flyby. For any given observation time  $t_{obs}$  we

341 calculate the corresponding simulation time as

$$t_{sim} = t_{sim,0} + \text{modulo}(t_{obs} - t_{obs,0}, t_{sim,1} - t_{sim,0}) \quad (1)$$

342 where  $t_{obs,0}$  is the reference observation time, which is essentially a free parameter. The  
 343 start time  $t_{sim,0}$  is set to 60s so that the initial transients (going from the approxi-  
 344 mate steady state into the time accurate simulation) are not included. The final time  
 345 is  $t_{sim,1} = 600$ s, so we use the remaining 9 minutes for both simulations. We note that  
 346 the simulations could be continued longer than 10 minutes, but that would not add much  
 347 extra information. Instead, we used the limited computational resources to do multiple  
 348 runs with different parameters as discussed in section 4.

349 Figures 9 and 10 show the Galileo observations compared with data extracted from the  
 350 Hall MHD and MHD-EPIC simulations using  $t_{obs,0} = 952.75$  min. The crosses on the bot-  
 351 tom panels show where  $t_{sim} = t_{sim,0}$ . While the Hall MHD simulation shows a reasonable  
 352 agreement with the smooth variation of the observed data, the small time scale variations  
 353 are quite different. The Hall MHD solution shows a high frequency (about 10 second  
 354 period) oscillation with fairly small amplitude between 948 min and 953 min observation  
 355 times corresponding to the inbound magnetopause crossing. The solution is relatively  
 356 smooth through the outbound magnetopause crossing. In contrast, the measured mag-  
 357 netic field varies on time scales ranging from seconds to about a minute or two. Figure 10  
 358 shows that the MHD-EPIC solution matches the observed variations much better, espe-  
 359 cially around the outbound magnetopause crossing between 960 min and 965 min. Both  
 360 the time scales and amplitudes agree reasonably well.

361 The Galileo data show a large amplitude (about 100 nT in the  $B_z$  component) and 1-  
 362 minute wide signal between  $t_{obs} = 962$  min and 963 min. Figure 11 shows a cut plane at

363  $Z = 0.83 R_G$  through the MHD-EPIC simulation at  $t_{sim} = 190 s$ , which approximately  
 364 corresponds to where the outbound  $B_z$  peak is found in the synthetic satellite data as  
 365 shown in the bottom panel of Figure 10 at  $t_{obs} \approx 964$  min. Galileo's actual trajectory  
 366 is shown with the dashed black line, while the stretched trajectory, where the data are  
 367 extracted from the simulation, is shown by the solid black line. The  $Z = 0.82 R_G$  value  
 368 is 1.06 times the  $z$  coordinate of the actual trajectory, which was approximately  $0.77 R_G$   
 369 at this time. There is a wound up field in the  $B_x$  and  $B_y$  components along the stretched  
 370 trajectory at around  $y = 1.3 R_G$ . Figure 12 shows a 3D visualization of the magnetic field  
 371 lines (colored with pressure) at the same time from two different view points. The mag-  
 372 netic field lines form two separate flux ropes, one of them intersecting Galileo's trajectory  
 373 shown by the gray tube. This flux rope is approximately perpendicular to the meridiional  
 374 ( $Y = 0$ ) plane where it is near the equatorial plane ( $Z = 0$ ), but at the intersection with  
 375 the Galileo trajectory ( $Z \approx 0.8$ ) its direction changes by almost 90 degrees, so it is roughly  
 376 aligned with the  $Z$  axis. This explains why the  $B_x$  and  $B_y$  components are wound up in  
 377 the  $Z = 0.82$  plane shown in Figure 11.

378 The 3D field line structure clearly indicates that the MHD-EPIC simulation produced  
 379 a Flux Transfer Event (FTE). Figure 13 shows a comparison of the Galileo data and the  
 380 MHD-EPIC results zoomed in for the outbound time interval (same curves were shown  
 381 in Figure 10 for a longer time interval). Galileo crossed the magnetopause at around  
 382 961.9 min, while in the simulation the crossing occurs at about 962.5 min as shown by  
 383 the  $B_z$  crossing from positive to negative values. About 0.3 min after the crossing the  
 384  $B_x$  component rises by about 50 nT from a minimum of  $-20$  nT for Galileo and  $-10$  nT  
 385 for the simulation, respectively. The  $B_x$  curves remain positive for about 0.5 min in the

Galileo observations, and about 1.5 min in the simulation. During the same interval, the  $B_y$  components are mostly positive with some oscillations between 0 and 50 nT. In both cases, the  $B_z$  component has a large peak in the last minute of the event with an amplitude of about 100 nT relative to the value outside the magnetosphere, which is  $-110$  nT and  $-70$  nT in the Galileo data and the MHD-EPIC results, respectively. Although we cannot expect quantitative agreement, the similarities between the observed and simulated magnetic features are quite striking. Based on the overall similarities, we conclude that Galileo has most likely observed a Flux Transfer Event during the outbound magnetopause crossing in this flyby.

To make the comparisons somewhat more quantitative, we calculated the power spectrum of the Galileo data and the time series extracted from the two simulations with the same parameters that were used for Figures 9 and 10. Figure 14 shows the comparison of the power spectra of the three components of the magnetic field. The frequency range is shown up to 0.3 Hz, because shorter frequencies are not meaningful given the discrete time resolution (the model output is saved at every second of simulation time). The agreement between the Galileo and MHD-EPIC power spectra are excellent, while the Hall MHD power spectra are quite different, with much less power in the higher frequencies.

#### 4. Additional Simulations

We made several additional runs to check how the results depend on various parameters. Here we briefly describe these runs and the conclusions made from them with respect to the reference Hall MHD and Hall MHD-EPIC runs presented in the previous section. A more in depth analysis and additional runs are deferred to a future paper.

407 We tried an MHD-EPIC simulation with BATS-R-US solving the ideal MHD (instead  
408 of Hall MHD) equations. Although the simulation worked for a reasonably long period,  
409 eventually an instability developed at the MHD-PIC boundary and the iPIC3D code  
410 crashed with unphysically large pressure and correspondingly large thermal velocities.  
411 We do not conclude that Hall MHD is a requirement for MHD-EPIC, but it seems to  
412 matter whether the PIC region is coupled with an ideal or a Hall MHD code.

413 As shown in the previous section, the pure Hall MHD reference simulation showed much  
414 smoother results than the MHD-EPIC simulation. A possible reason for this can be the  
415 numerical diffusion due to the finite grid resolution. We did a high resolution Hall MHD  
416 run with  $1/64 R_G$  grid resolution near the moon using about 50 million grid cells in total.  
417 The time step was reduced to  $\Delta t = 0.01$  s (from 0.025 s). The overall large scale solution  
418 of this high resolution simulation is quite similar to the coarser Hall MHD results. The  
419 out-of-plane  $B_y$  field remains similar to that shown on the left of Figure 4, with a slightly  
420 increased amplitude but still much narrower in the X direction than the MHD-EPIC  
421 solution shown in the right panel. The density inside the magnetosphere also remains  
422 lower than for the MHD-EPIC solution, similar to the results shown in Figures 6 and 7.  
423 On the other hand, the solution became much more dynamic at this twice higher grid  
424 resolution, and the Hall MHD simulation shows FTEs on the upstream side as well as  
425 repeated plasmoid formation in the tail. The magnetic field extracted along the Galileo  
426 orbit shows dynamic features both at the inbound and outbound times. The FFT power  
427 spectrum of the extracted synthetic magnetic field observation is very similar to the Galileo  
428 data. We conclude that the small scale features of the Hall MHD results are sensitive to  
429 the grid resolution. We note that the high resolution Hall MHD simulation was much

430 more expensive than the original simulation, and it required 4.9 hours on 1920 cores, or  
431 about 9,500 core-hours to model one minute of simulation time, that is about 16 times  
432 more than the coarser run.

433 We also did a Hall MHD-EPIC simulation using a single upstream PIC region with  
434  $1/64 R_G$  grid resolution, so the  $112 \times 368 \times 300$  grid consist of about 12 million cells.  
435 To reduce the memory used by iPIC3D, the number of macroparticles were set to 125  
436 ions and 125 electrons (instead of 216), so the total number of particles is about 3 billion  
437 initially. There are 8 times more grid cells and about 4.6 times more particles per unit  
438 volume than in the reference MHD-EPIC simulation, so the errors due to finite number  
439 of cells and particles in the PIC domain should reduce substantially. The time step had  
440 to be reduced to  $\Delta t = 0.005$  s to maintain stability. The BATS-R-US grid was kept  
441 the same as in the baseline runs with  $1/32 R_G$  cell size in the most refined part of the  
442 grid. This run demonstrates that the MHD-EPIC algorithm works even if the MHD  
443 and PIC grids are not the same. It also demonstrates that the PIC regions do not have  
444 to cover the whole magnetosphere to obtain a meaningful simulation. Even with these  
445 adjustments, the high resolution run required about 24,000 core hours to simulate 1 minute  
446 of simulation time (about 10 times more than the reference MHD-EPIC run). We found  
447 that the solution inside the upstream PIC region did not change significantly relative to  
448 the reference solution obtained with  $1/32 R_G$  resolution. There are a few FTE-like events  
449 reminiscent of the observations, and the FFT spectrum remains close to the observations.  
450 Figure 15 shows a flux rope crossing the  $Y = 0$  plane close to the equatorial plane similar  
451 to the flux rope obtained in the reference MHD-EPIC simulation shown in Figure 12.  
452 Note, however, that the helicity of this flux rope is positive and it bends towards  $-Z$

453 for positive  $Y$ , while the flux rope in Figure 12 has a mostly negative helicity and bends  
 454 toward  $+Z$  for positive  $Y$ . Figure 16 shows the electron number density, magnetic field  
 455 lines, and the direction of the electric field in the  $Y = 0$  cut through the PIC region.  
 456 The electron density is enhanced inside the flux rope. Figure 17 shows the electron and  
 457 ion distribution functions obtained by iPIC3D in the vicinity of the flux rope. The phase  
 458 space density is binned by the X coordinate and the three components of velocity both for  
 459 electrons and ions. There is a significant electron heating inside the flux rope as shown  
 460 by the enhanced width of the electron velocity distribution function near  $x \approx 2.5$  Mm.  
 461 The ion distribution function shows some anisotropy: the thermal widths of the X and Y  
 462 components of the velocity are the largest and smallest, respectively.

463 Galileo observations [*Kivelson et al.*, 2004] show that the Jovian plasma consists of  
 464 a mixture of a thermal population and a hot ion population. The number density is  
 465 dominated by the thermal population while the thermal pressure is dominated by the  
 466 hot ions. Both populations are a mixture of hydrogen and oxygen ions. We performed  
 467 an MHD-EPIC simulation using only the thermal ion population with the mass density  
 468  $\rho = 56 m_p/\text{cm}^{-3}$  but the total Jovian wind pressure is set to  $p_i = 0.2$  nPa (instead of  
 469 3.8 nPa) with  $p_e = p_i/5$ . The BATS-R-US grid was the same as in the reference MHD-  
 470 EPIC simulation, but only 2 PIC regions were used: the upstream and tail regions with  
 471 the  $1/32 R_G$  grid resolution. To maintain stability we had to reduce the time step to  
 472  $\Delta t = 0.005$  s, which made this simulation more expensive than the reference MHD-EPIC  
 473 simulation that used  $\Delta t = 0.025$  s. The overall structure of the magnetosphere changes  
 474 significantly due to the reduced thermal pressure of the incoming Jovian plasma. The  
 475 magnetopause moved further out because of the weaker upstream pressure, so we had to

476 increase the stretch factor of the Galileo trajectory from 1.06 to 1.14. Even with this  
477 increased stretch factor the smooth part of the magnetic field does not agree too well  
478 with the observed fields because the field observed along the Galileo trajectory during  
479 this pass is very sensitive to both the size and the shape of the magnetosphere, which  
480 changes in response to variations of the upstream pressure. Nevertheless, the simulation  
481 produced a few FTEs that looked remarkably similar to the observed data as shown in  
482 Figure 18. This implies that the energy distribution of the Jovian plasma does not make  
483 a huge difference in the FTE formation. In the future, however, we plan to do simulations  
484 with separate hot and thermal ion components. This will require extending the coupler  
485 to multi-ion Hall MHD-EPIC.

486 Finally, we also examined what causes the strong bending of the flux rope as it extends  
487 from the equatorial plane up to the  $Z = 0.8$  plane near the Galileo trajectory. The  
488 symmetry with respect to the equatorial plane is broken by the tilt of the internal dipole  
489 and the electric field caused by the  $B_y$  component of the incoming Jovian magnetic field.  
490 We performed a simulation with the dipole aligned with the  $Z$  axis and  $B_y = 0$  for the  
491 Jovian magnetic field. Although this  $\pm Z$  symmetric run also showed reconnection island  
492 formation in the  $Y = 0$  plane, no extended flux ropes were formed. For this symmetric  
493 case the synthetic Galileo data does not show any FTE signatures, and the FFT power  
494 spectrum has a lower magnitude than what is observed. The simulations suggest that flux  
495 ropes are more likely to form with a guide field ( $B_y$  component) and the bending is most  
496 likely caused by the kink instability. We note, however, that the helicity of the flux rope  
497 is not determined by the  $B_y$  component in a straightforward manner. The simulations  
498 contain flux ropes with both positive and negative helicities.



## 5. Conclusion

499 We have successfully modeled Ganymede's magnetosphere with the new two-way cou-  
500 pled MHD-EPIC model. The embedded PIC regions fully covered the parts of the system  
501 where kinetic effects are likely to be important, so in effect we have produced the first  
502 fully kinetic and reasonably well resolved numerical model of a global magnetosphere.  
503 The role of the Hall MHD model (driven by the Jovian wind values at the distant outer  
504 boundaries) is to calculate the proper boundary conditions for the PIC model, and to  
505 properly propagate away the perturbations generated by the PIC model. In addition, the  
506 Hall MHD code also couples the four PIC regions together, because currently we cannot  
507 use a single continuous PIC region to cover all the reconnection sites due to the limita-  
508 tions of the PIC grid (Cartesian box) and the presence of the moon in the middle. Since  
509 most of the interesting dynamics is happening inside the upstream PIC region, and since  
510 there are no obvious numerical artifacts between the PIC regions, we are fairly confident  
511 that the results are not strongly affected by this approximation. In the future, however,  
512 we plan to improve the scheme by implementing direct communication between the PIC  
513 regions.

514 Our simulations show that the Hall MHD-EPIC model can simulate the dynamics of  
515 Ganymede's magnetosphere for the relevant global time scales. The numerical scheme  
516 works robustly, and there are no significant numerical artifacts. In fact, the Hall MHD  
517 and Hall MHD-EPIC models provide remarkably similar solutions, which confirms the  
518 importance of ion scale physics that is captured by both models (but not by ideal MHD, see  
519 *Dorelli et al.* [2015]). The similarity also implies that the MHD-EPIC coupling algorithm  
520 works well and there are no significant numerical artifacts. There are also significant

521 differences that we attribute to the additional kinetic physics in the PIC model, such as  
522 finite Larmor radius effects, non-Maxwellian distribution functions, etc. We find that the  
523 PIC model gives a more dynamic solution as evidenced by the quasi-periodic formation of  
524 large FTEs at the upstream magnetopause. In comparison the Hall MHD solution with  
525 the same grid resolution is less dynamic in this region. The Hall MHD solution, on the  
526 other hand, shows very clear signs of the Kelvin-Helmholtz instability in one quadrant of  
527 equatorial plane. The Hall MHD-EPIC model also shows oscillations in the same region,  
528 but the wavelength and the amplitude are smaller. We also find significant differences in  
529 the density and pressure distributions near Ganymede.

530 Comparison with the magnetic measurements of the Galileo spacecraft shows that there  
531 is a slight difference of about 6% between the observed and modeled magnetopause dis-  
532 tances. There can be various reasons for this, including changes in the upstream Jovian  
533 wind conditions during the flyby and the representation of the inner boundary at the  
534 surface of the moon as a simple absorbing body with a fixed radial magnetic field. We  
535 plan to improve the description of the inner boundary by modeling the moon as a layered  
536 finite conductivity body. We expect that letting the magnetic field propagate into the  
537 body will reduce the simulated magnetopause distance in agreement with observations.  
538 This approach has been successfully used for Ganymede [*Jia et al.*, 2008] and recently for  
539 Mercury [*Jia et al.*, 2015].

540 The MHD-EPIC simulation produced an FTE that shows good agreement with the  
541 Galileo observations. The temporal width, the shapes and magnitudes of the magnetic  
542 signatures in the three components of the magnetic field all resemble surprisingly well  
543 the observed FTE signatures. We only had one free parameter that could be adjusted,

544 the relative time shift between the simulation and the observations. Looking at the 3D  
 545 structure of the FTEs reveals that the flux ropes can bend significantly and therefore  
 546 exhibit complex magnetic geometries. Near the equatorial plane the flux ropes are roughly  
 547 aligned with the Y axis, but near the Galileo trajectory at  $Z \approx 0.8 R_G$  the same flux rope  
 548 can be more-or-less aligned with the Z axis. This means that the interpretation of the in  
 549 situ magnetic measurements is not straightforward at all. The comprehensive 3D MHD-  
 550 EPIC model can provide the context and strongly suggest that Galileo observed an FTE  
 551 indeed.

552 We also calculated the power spectra of the three magnetic components and found that  
 553 the spectra of the observed and MHD-EPIC simulated fields are very similar, while the  
 554 Hall MHD spectra deviate significantly with much less power in the higher frequencies.  
 555 Increasing the grid resolution significantly improved the agreement with small scale fluc-  
 556 tuations for the Hall MHD model, but it did not make much difference for the MHD-EPIC  
 557 model.

558 The embedded kinetic model can provide detailed information about the electron and  
 559 ion distribution functions. Figure 17 demonstrates this capability, and shows that there is  
 560 significant heating inside the flux rope as also predicted by pure kinetic, mostly 2D, sim-  
 561 ulations [Drake *et al.*, 2006]. We defer the more detailed analysis to a future publication.

562 Finally, we provide some information on the computational efficiency. All simulations  
 563 (with the exception of the high resolution Hall MHD run) were done on 960 CPU cores.  
 564 For the standard grid simulating 1 minute of physical time takes about 0.3 hours wall  
 565 clock time for resistive MHD, 0.6 hours for Hall MHD, and 2.4 hours for MHD-EPIC. If  
 566 we tried to simulate the whole  $(256 R_G)^3$  domain with iPIC3D using the same  $1/32 R_G$

567 grid resolution, it would require 500 billion PIC grid cells with 237 trillion macroparticles.  
568 Even assuming perfect parallel scaling, it would take about 20,000 CPU core years (not  
569 hours) to simulate a single minute of physical time, which is clearly not feasible and/or  
570 economical.

571 Our model is the first global kinetic model of a complete magnetosphere, but of course  
572 there are still some simplifications. In the Hall MHD model the Jovian wind was assumed  
573 to have a Maxwellian distribution and the electron pressure was taken to be one fifth of  
574 the ion pressure. In the future we will do runs where we distinguish between the thermal  
575 and hot ion populations and solve for the electron pressure in the Hall MHD model and  
576 couple it with iPIC3D. Direct coupling between the PIC regions will also be implemented.  
577 The representation of the inner boundaries will be improved by using a resistive body.

578 **Acknowledgments.** GT was partially supported by the Space Hazards Induced near  
579 Earth by Large, Dynamic Storms (SHIELDS) project DE-AC52-06NA25396, funded by  
580 the U.S. Department of Energy through the Los Alamos National Laboratory Directed  
581 Research and Development program and also by the INSPIRE NSF grant PHY-1513379.

582 XJ acknowledges support by the NASA Solar System Workings program through  
583 grant NNX15AH28G and the Heliophysics Supporting Research program through grant  
584 NNX15AJ68G.

585 Computational resources supporting this work were provided by the NASA High-End  
586 Computing (HEC) Program through the NASA Advanced Supercomputing (NAS) Divi-  
587 sion at Ames Research Center and from Yellowstone ([ark:/85065/d7wd3xhc](http://ark:/85065/d7wd3xhc)) provided by  
588 NCAR's Computational and Information Systems Laboratory, sponsored by the National  
589 Science Foundation.

590 The SWMF code (including BATS-R-US and iPIC3D) is publicly available through the  
591 csem.engin.umich.edu/tools/swmf web site after registration. The output of the simula-  
592 tions presented in this paper can be obtained by contacting the first author GT.

## References

- 593 Daldorff, L. K. S., G. Toth, T. I. Gombosi, G. Lapenta, J. Amaya, S. Markidis, and  
594 J. U. Brackbill (2014), Two-way coupling of a global Hall magnetohydrodynamics  
595 model with a local implicit Particle-in-Cell model, *J. Comput. Phys.*, *268*, 236, doi:  
596 10.1016/j.jcp.2014.03.009.
- 597 Dedner, A., F. Kemm, D. Kröner, C. Munz, T. Schnitzer, and M. Wesenberg (2003),  
598 Hyperbolic divergence cleaning for the MHD equations, *J. Comput. Phys.*, *175*, 645–  
599 673.
- 600 Dorelli, J. C., A. Gloer, G. Collinson, and G. Toth (2015), The role of the hall effect in  
601 the global structure and dynamics of planetary magnetospheres: Ganymede as a case  
602 study, *JGR*, *120*, 5377–5392, doi:10.1002/2014JA020951.
- 603 Drake, J. F., M. Swisdak, H. Che, and M. A. Shay (2006), Electron accelera-  
604 tion from contracting magnetic islands during reconnection, *Nature*, *443*, 553, doi:  
605 10.1038/nature05116.
- 606 Duling, S., J. Saur, and J. Wicht (2014), Consistent boundary conditions at nonconducting  
607 surfaces of planetary bodies: Applications in a new ganymede mhd model, *J. Geophys.*  
608 *Res.*, *119*, 4412–4440, doi:10.1002/2013JA019554.
- 609 Jia, X. (2015), Satellite magnetotails, in *Magnetotails in the Solar System*, edited by  
610 A. Keiling, C. M. Jackman, and P. A. Delamere, AGU Geophysical Monograph Series,

- 611 John Wiley & Sons, doi:10.1002/9781118842324.ch8.
- 612 Jia, X., R. J. Walker, M. G. Kivelson, K. K. Khurana, and J. A. Linker (2008), Three-  
613 dimensional MHD simulations of Ganymede's magnetosphere, *J. Geophys. Res.*, *113*,  
614 A06,212, doi:10.1029/2007JA012748.
- 615 Jia, X., R. J. Walker, M. G. Kivelson, K. K. Khurana, and J. A. Linker (2009), Properties  
616 of ganymede's magnetosphere inferred from improved three-dimensional mhd simula-  
617 tions, *J. Geophys. Res.*, *114*, A09,209, doi:10.1029/2009JA014375.
- 618 Jia, X., R. J. Walker, M. G. Kivelson, K. K. Khurana, and J. A. Linker (2010), Dynamics of  
619 ganymede's magnetopause: Intermittent reconnection under steady external conditions,  
620 *J. Geophys. Res.*, *115*, A12,202, doi:10.1029/2010JA015771.
- 621 Jia, X., J. A. Slavin, T. I. Gombosi, L. K. S. Daldorff, G. Toth, and B. van der Holst  
622 (2015), Global MHD simulations of Mercury's magnetosphere with coupled planetary  
623 interior: Induction effect of the planetary conducting core on the global interaction, *J.*  
624 *Geophys. Res.*, *120*, 4763–4775, doi:10.1002/2015JA021143.
- 625 Kivelson, M., K. Khurana, F. Coroniti, S. Joy, C. Russell, R. Walker, J. Warnecke, L. Ben-  
626 nett, and C. Polanskey (1997), Magnetic field and magnetosphere of Ganymede, *Geo-*  
627 *phys. Res. Lett.*, *24*, 2155.
- 628 Kivelson, M. G., J. Warnecke, L. Bennett, S. Joy, K. Khurana, J. A. Linker, C. Russell,  
629 R. J. Walker, and C. Polanskey (1998), Ganymede's magnetosphere: Magnetometer  
630 overview, *J. Geophys. Res.*, *103*(E9), 19,963, doi:10.1029/98JE00227.
- 631 Kivelson, M. G., K. K. Khurana, and M. Volwerk (2002), The permanent and inductive  
632 magnetic moments of ganymede, *Icarus*, *157*, 507–522.

- 633 Kivelson, M. G., F. Bagenal, F. M. Neubauer, W. Kurth, C. Paranicas, and J. Saur  
634 (2004), Magnetospheric interactions with satellites, in *Jupiter: The Planet, Satellites  
635 and Magnetosphere*, edited by F. Bagenal, T. E. Dowling, and W. B. McKinnon, pp.  
636 513–536, Cambridge Univ. Press, Univ. of Colo., Cambridge.
- 637 Kopp, A., and W.-H. Ip (2002), Resistive MHD simulations of Ganymede's magnetosphere  
638 2. Time variabilities of the magnetic field topology, *J. Geophys. Res.*, *107*(A12), 1490,  
639 doi:10.1029/2001JA005071.
- 640 Lapenta, G., S. Markidis, A. Divin, M. Goldman, and D. Newman (2010), Scales of guide  
641 field reconnection at the hydrogen mass ratio, *Physics of Plasmas*, *17*(8), 082,106, doi:  
642 10.1063/1.3467503.
- 643 Liljeblad, E., T. Sundberg, T. Karlsson, and A. Kullen (2014), Statistical investigation  
644 of Kelvin-Helmholtz waves at the magnetopause of mercury, *J. Geophys. Res.*, *119*,  
645 9670–9683, doi:10.1002/2014JA020614.
- 646 Markidis, S., G. Lapenta, and Rizwan-Uddin (2010), Multi-scale simulations of  
647 plasma with ipic3d, *Mathematics and Computers in Simulation*, *80*, 1509–1519, doi:  
648 10.1016/j.matcom.2009.08.038.
- 649 Neubauer, F. M. (1998), The sub-Alfvénic interaction of the Galilean satellites with the  
650 Jovian magnetosphere, *J. Geophys. Res.*, *103*, 19,843–19,866, doi:10.1029/97JE03370.
- 651 Paty, C., and R. Winglee (2004), Multi-fluid simulations of ganymede's magnetosphere,  
652 *Geophys. Res. Lett.*, *31*, L24,806, doi:10.1029/2004GL021220.
- 653 Paty, C., W. Paterson, and R. Winglee (2008), Ion energization in Ganymede's magneto-  
654 sphere: Using multifluid simulations to interpret ion energy spectrograms, *J. Geophys.  
655 Res.*, *113*, 6211, doi:10.1029/2007JA012848.

**Figure 1.** Meridional cut through the tail PIC region showing the X components of the ion (top) and electron (bottom) bulk velocities in km/s and the magnetic field lines (white lines). The coordinates are given in units of Ganymede radius  $R_G$ . The electron jets extending from the X-line are clearly visible. Note that the color scales are different for the two panels.

656 Powell, K., P. Roe, T. Linde, T. Gombosi, and D. L. De Zeeuw (1999), A solution-adaptive  
657 upwind scheme for ideal magnetohydrodynamics, *J. Comp. Phys.*, *154*, 284–309.

658 Powell, K. G. (1994), An approximate Riemann solver for magnetohydrodynamics (that  
659 works in more than one dimension), *Tech. Rep. 94-24*, Inst. for Comput. Appl. in Sci.  
660 and Eng., NASA Langley Space Flight Center, Hampton, Va.

661 Ricci, P., G. Lapenta, and J. U. Brackbill (2002), Gem reconnection challenge: Implicit  
662 kinetic simulations with the physical mass ratio, *Geophys. Res. Lett.*, *29*, 2088, doi:  
663 10.1029/2002GL015314.

664 Tóth, G., et al. (2005), Space Weather Modeling Framework: A new tool for the space  
665 science community, *J. Geophys. Res.*, *110*, A12,226, doi:10.1029/2005JA011126.

666 Tóth, G., D. L. De Zeeuw, T. I. Gombosi, and K. G. Powell (2006), A parallel ex-  
667 plicit/implicit time stepping scheme on block-adaptive grids, *J. Comput. Phys.*, *217*,  
668 722–758, doi:10.1016/j.jcp.2006.01.029.

669 Tóth, G., Y. J. Ma, and T. I. Gombosi (2008), Hall magnetohydrodynamics on block  
670 adaptive grids, *J. Comput. Phys.*, *227*, 6967–6984, doi:10.1016/j.jcp.2008.04.010.

671 Tóth, G., et al. (2012), Adaptive numerical algorithms in space weather modeling, *J.*  
672 *Comput. Phys.*, *231*, 870–903, doi:10.1016/j.jcp.2011.02.006.



**Figure 2.** Meridional (top) and equatorial (bottom) cuts showing the Hall MHD solution in the full computational domain. The white lines show the magnetic field lines (top) and streamlines (bottom), respectively. The color shows the 10 based logarithm of pressure in unit of nPa. The Alfvén wings and slow wave generated by Ganymede in the subsonic and sub-Alfvénic Jovian wind are clearly seen in the meridional cut. Note that the solution is essentially unperturbed near the outer boundaries.

**Figure 3.** Meridional (top) and equatorial (bottom) cuts showing the location of the PIC regions (black rectangles). The white lines represent the magnetic field lines (top) and streamlines (bottom), respectively. The colors show the Y component of the current density in units of  $\mu\text{A}/\text{m}^2$ .

**Figure 4.** Meridional cuts of the Hall MHD (left) and Hall MHD-EPIC (right) solutions at  $t = 350$  s. The white lines trace the  $B_x$  and  $B_z$  components of the magnetic field. The colors show the out-of-plane component  $B_y$  in units of nT. The black rectangles indicate the edges of the upstream and downstream PIC regions.

**Figure 5.** Equatorial cuts of the Hall MHD (left) and Hall MHD-EPIC (right) solutions at  $t = 350$  s. The white lines trace the  $u_x$  and  $u_y$  components of the velocity. The colors show the magnitude of the current density  $J$  in units of  $\mu\text{A}/\text{m}^2$ . The red rectangles indicate the edges of the four PIC regions.

**Figure 6.** Meridional cuts of the Hall MHD (left) and Hall MHD-EPIC (right) solutions at  $t = 350$  s showing the mass density (top) and pressure (bottom). The black rectangles in the bottom right panel indicate the edges of the upstream and downstream PIC regions for the MHD-EPIC simulation.

**Figure 7.** Equatorial cuts of the Hall MHD (left) and Hall MHD-EPIC (right) solutions at  $t = 350$  s showing the mass density (top) and pressure (bottom). The black rectangles in the bottom right panel indicate the edges of the four PIC regions for the MHD-EPIC simulation.

**Figure 8.** Comparison of the observed (black line) and simulated (blue line) magnetic field along the Galileo trajectory at an arbitrary simulation time (400 s) in the MHD-EPIC simulation. The red line shows the simulated values along a slightly modified trajectory that is obtained from the original by multiplying the trajectory coordinates with 1.06. The observation time on the horizontal axis is measured in minutes relative to 00 UT of May 7, 1997.

**Figure 9.** Comparison of the observed (black line) and Hall MHD (blue line) magnetic fields. The time series is extracted from the simulation that is repeated in a periodic fashion. The starting points of the periods are indicated by the crosses in the bottom panel.

**Figure 10.** Comparison of the observed (black line) and Hall MHD-EPIC (red line) magnetic fields. The time series is extracted from the simulation that is repeated in a periodic fashion. The starting points of the periods are indicated by the crosses in the bottom panel.

**Figure 11.** Cut plane at  $z = 0.83 R_G$  through the MHD-EPIC simulation at time  $t_{sim} = 190$  s. The colors show the out-of-plane magnetic field component  $B_z$ . The white lines follow the  $B_x$  and  $B_y$  components. The dashed black line is the projection of the original Galileo trajectory, while the solid line is the stretched trajectory used to extract the data for Figure 10. The modified trajectory goes through the middle of an FTE near the outbound crossing of the magnetopause. The spacecraft moved towards the positive Y direction.

**Figure 12.** 3D visualization of the magnetic field structure from the  $-X, +Z$  (top panel) and  $-Y, +Z$  (bottom panel) directions obtained by the MHD-EPIC simulation at time  $t_{sim} = 190$  s. The almost straight gray tube indicates the Galileo trajectory. The colored tubes show selected magnetic field lines colored by the pressure. The translucent equatorial plane is colored with the current density. Ganymede's surface is shown by the gray sphere.

**Figure 13.** Comparison of the observed (black line) and Hall MHD-EPIC (red line) magnetic fields near the outbound magnetopause crossing. The cross at 961.75 min in the bottom panel shows where the simulation time jumps from 600 s back to 60 s, which is outside the event. The observed and simulated fields show clear, and comparable, signature of Flux Transfer Events (FTEs).

**Figure 14.** Power spectra of the observed (black), Hall MHD (blue) and MHD-EPIC (red) simulated components of the magnetic field. The frequency grid has a 0.75 mHz spacing. The spectra are smoothed over 5 frequency points for sake of clarity.

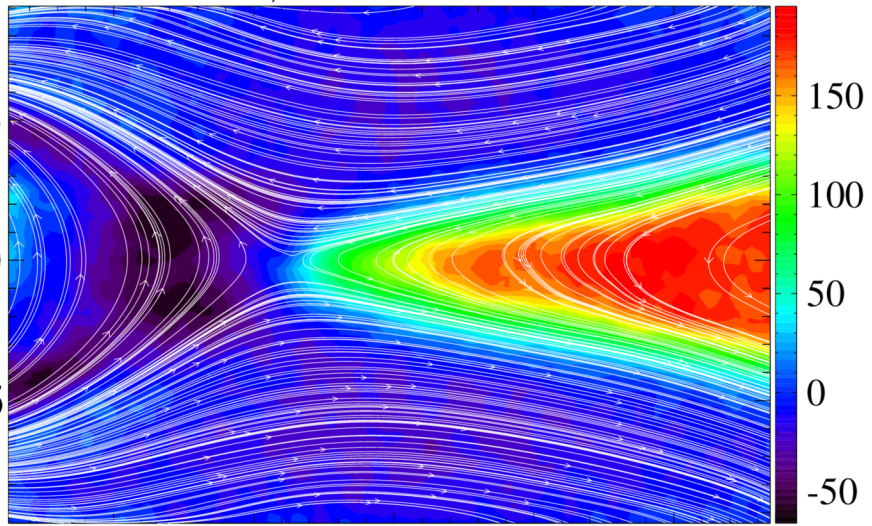
**Figure 15.** 3D visualization of the magnetic field structure from the  $-X, +Z$  direction obtained by the high resolution MHD-EPIC simulation with a single PIC region with  $1/64 R_G$  resolution at time  $t_{sim} = 180$  s. The almost straight gray tube indicates the Galileo trajectory. The colored tubes show selected magnetic field lines colored by the pressure. The translucent equatorial plane is colored with the current density. Ganymede's surface is shown by the gray sphere.

**Figure 16.**  $Y = 0$  cut through the PIC region of the high  $1/64 R_G$  resolution MHD-EPIC simulation at time  $t_{sim} = 180 s$  showing the electron number density (color contours) in units of  $\text{cm}^{-3}$ , the magnetic field lines (white lines) and the electric field directions (arrows). Coordinates are measured in meters relative to the corner of the PIC region. The black rectangle indicates the edges of the 3D box  $2.2 \text{ Mm} < x < 2.6 \text{ Mm}$ ,  $7.45 \text{ Mm} < y < 7.75 \text{ Mm}$ ,  $6.05 \text{ Mm} < z < 6.3 \text{ Mm}$  from which the distribution functions in Figure 17 are obtained.

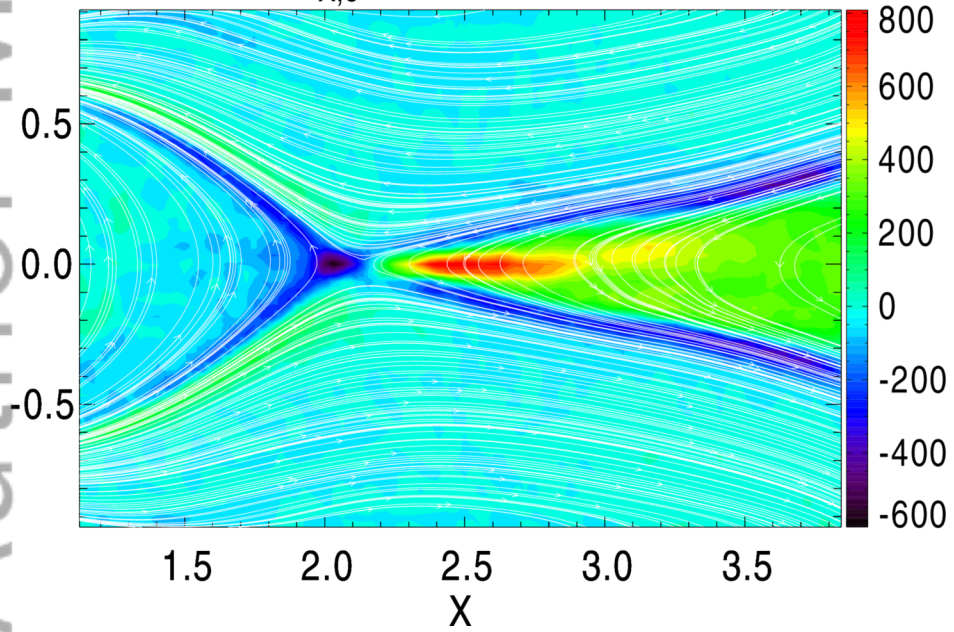
**Figure 17.** Electron and ion distribution functions binned by the X coordinate (measured in meters relative to the corner of the PIC region) and the three components of velocity (measured in  $\text{Mm/s}$ ) in a box near the flux rope as shown in Figure 16. The electron and ion phases space densities are normalized so that their integral over the 3D box and the velocity space is unity.

**Figure 18.** Comparison of the observed (black line) and Hall MHD-EPIC simulation with thermal Jovian ions only (red line) magnetic fields near the outbound magnetopause crossing. The cross at 963.9 min in the bottom panel shows where the simulation time jumps, which is clearly after the event. The observed and simulated fields show clear, and comparable, signatures of Flux Transfer Events (FTEs).

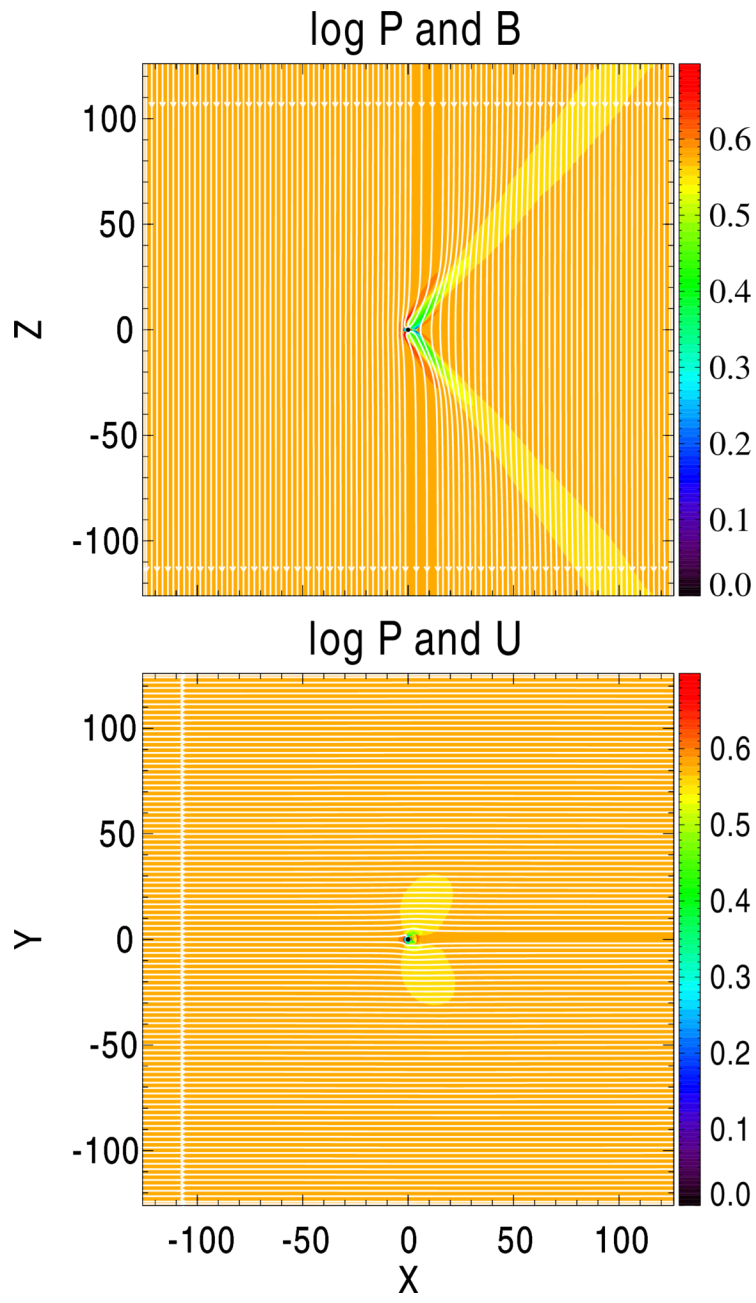
$U_{x,i}$  and field lines



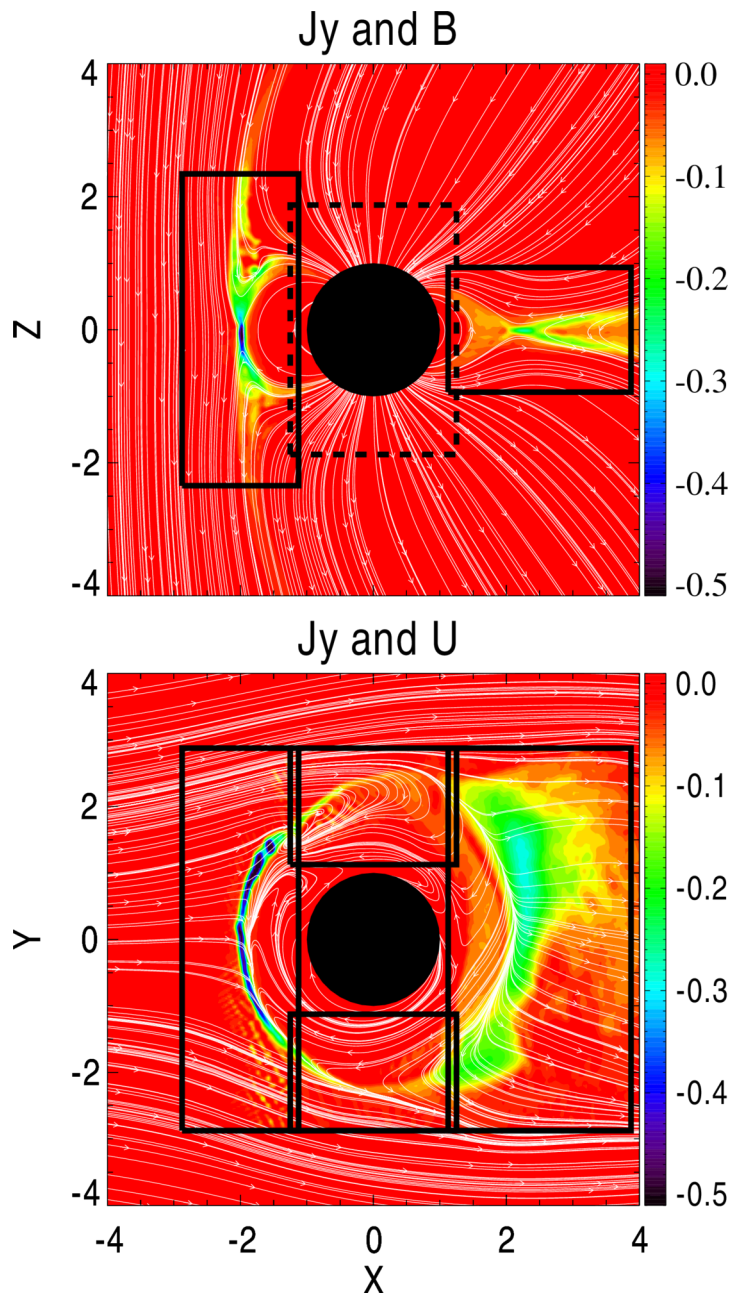
$U_{x,e}$  and field lines



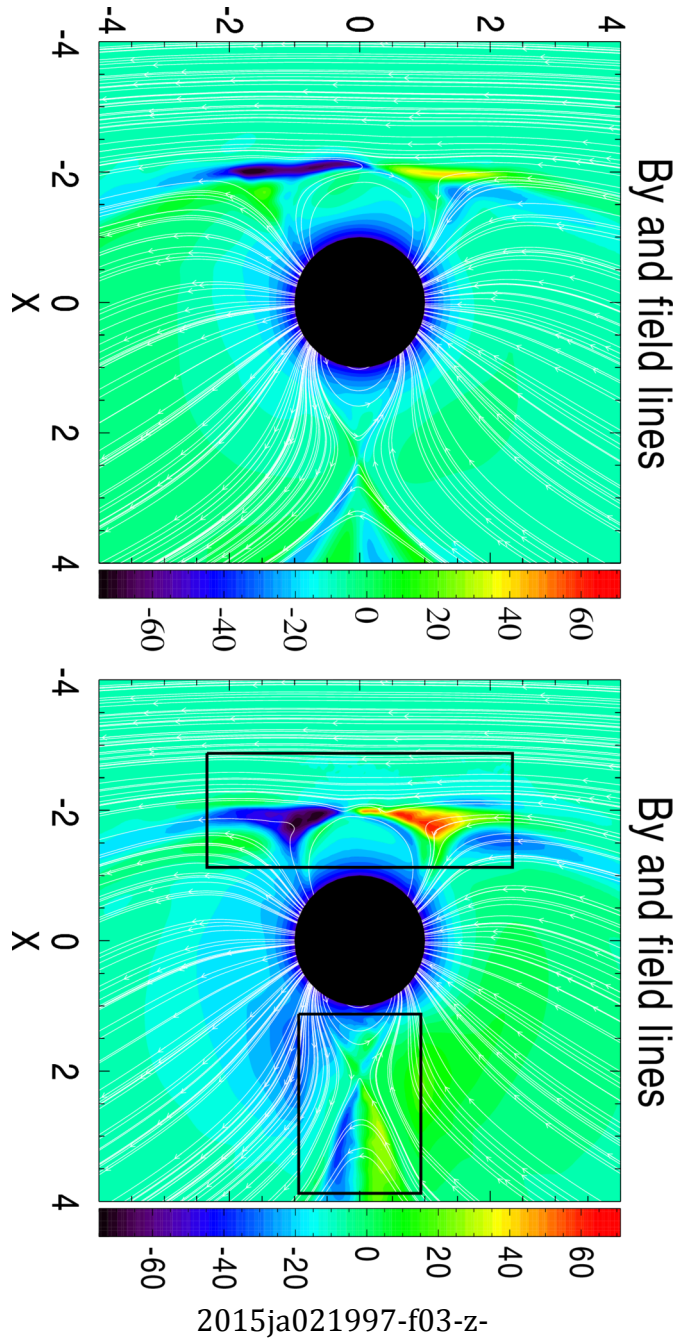
2015ja021997-f00-z-



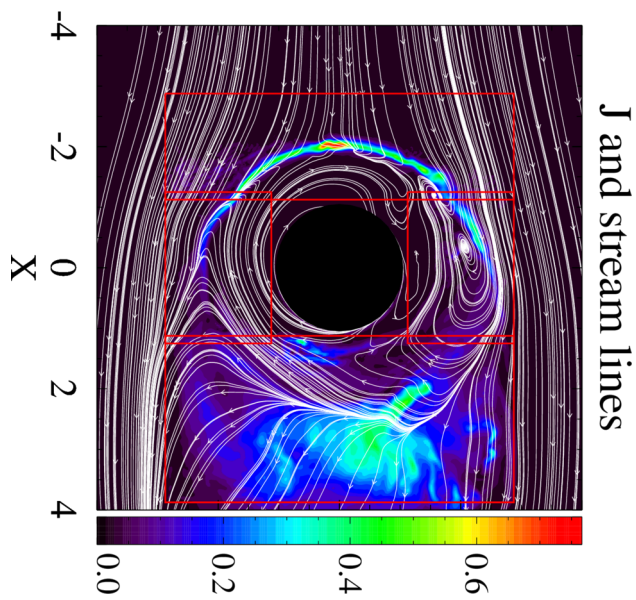
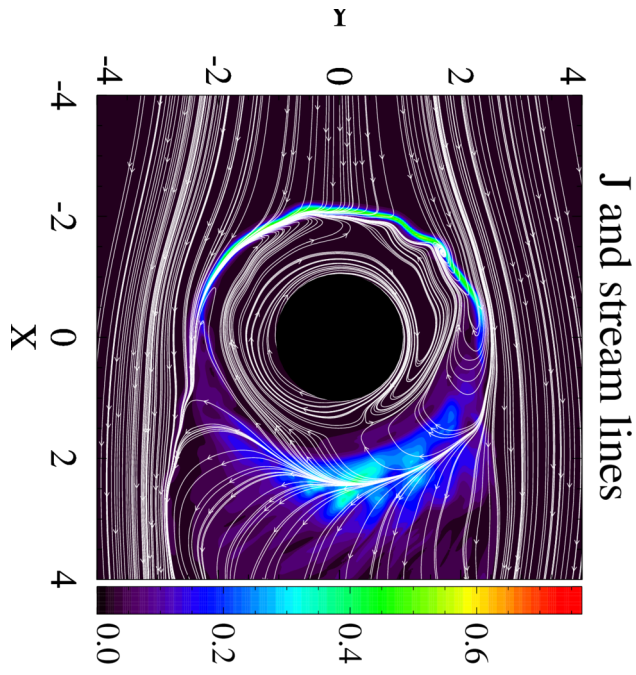
2015ja021997-f01-z-



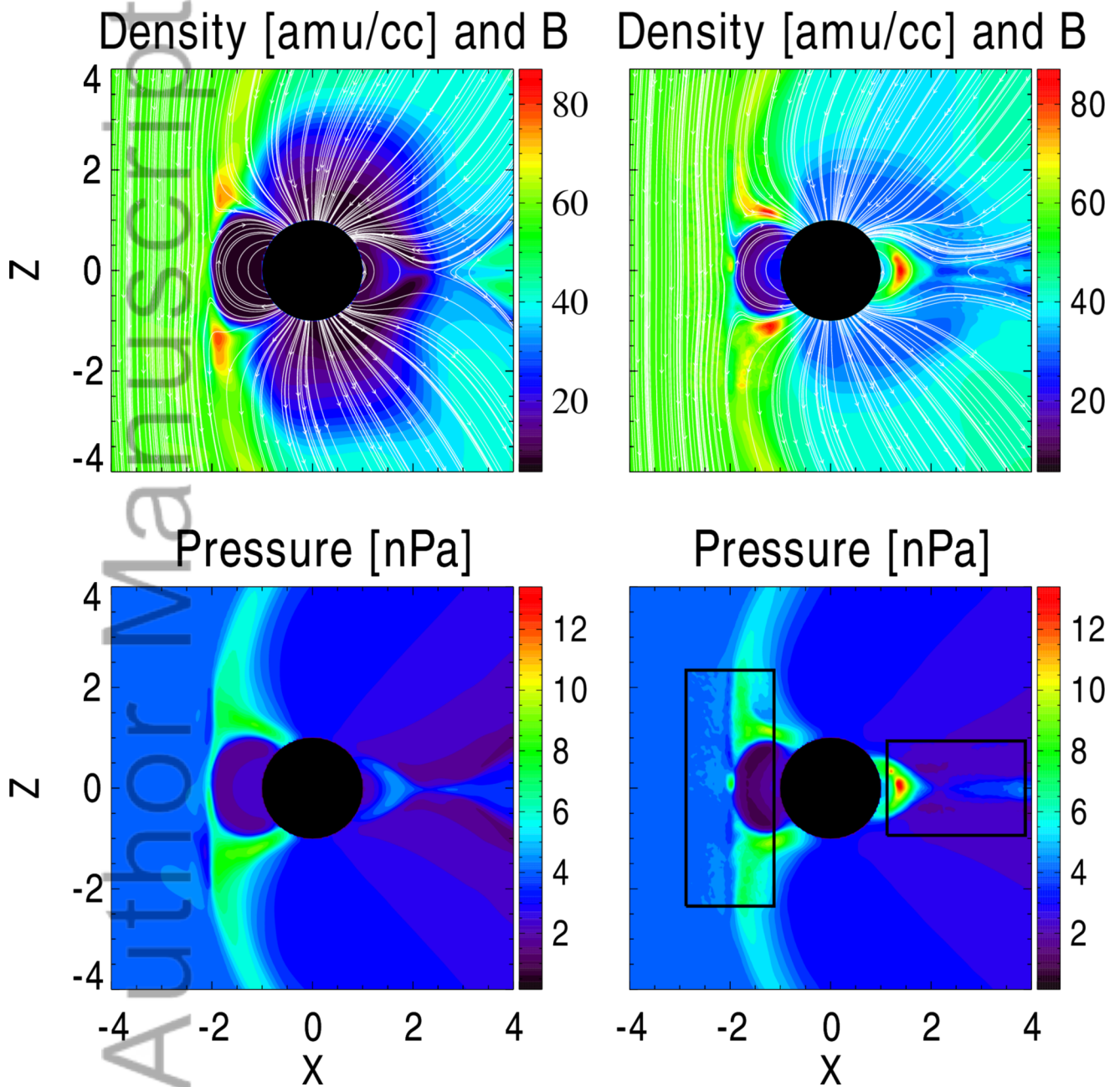
2015ja021997-f02-z-



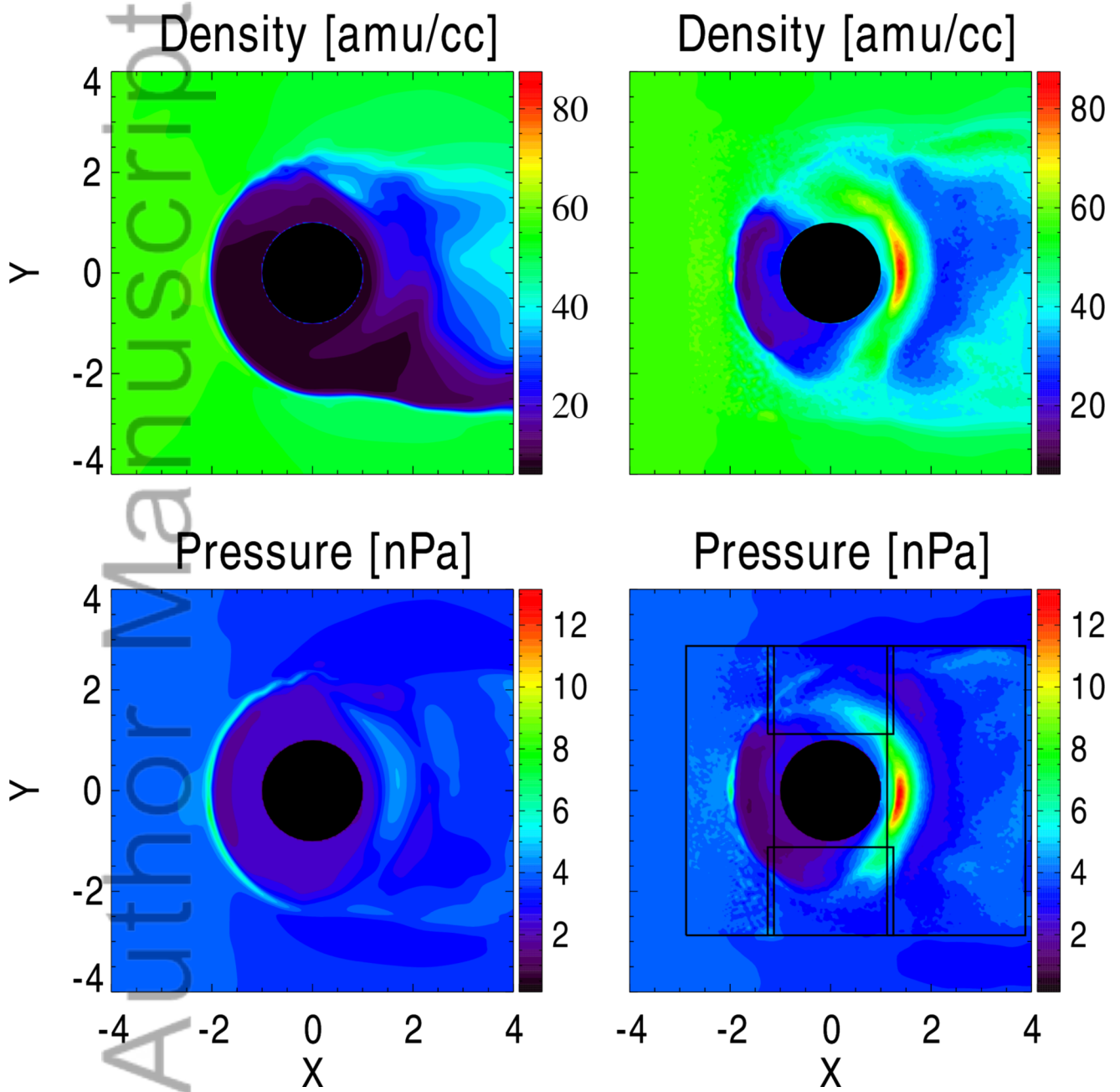




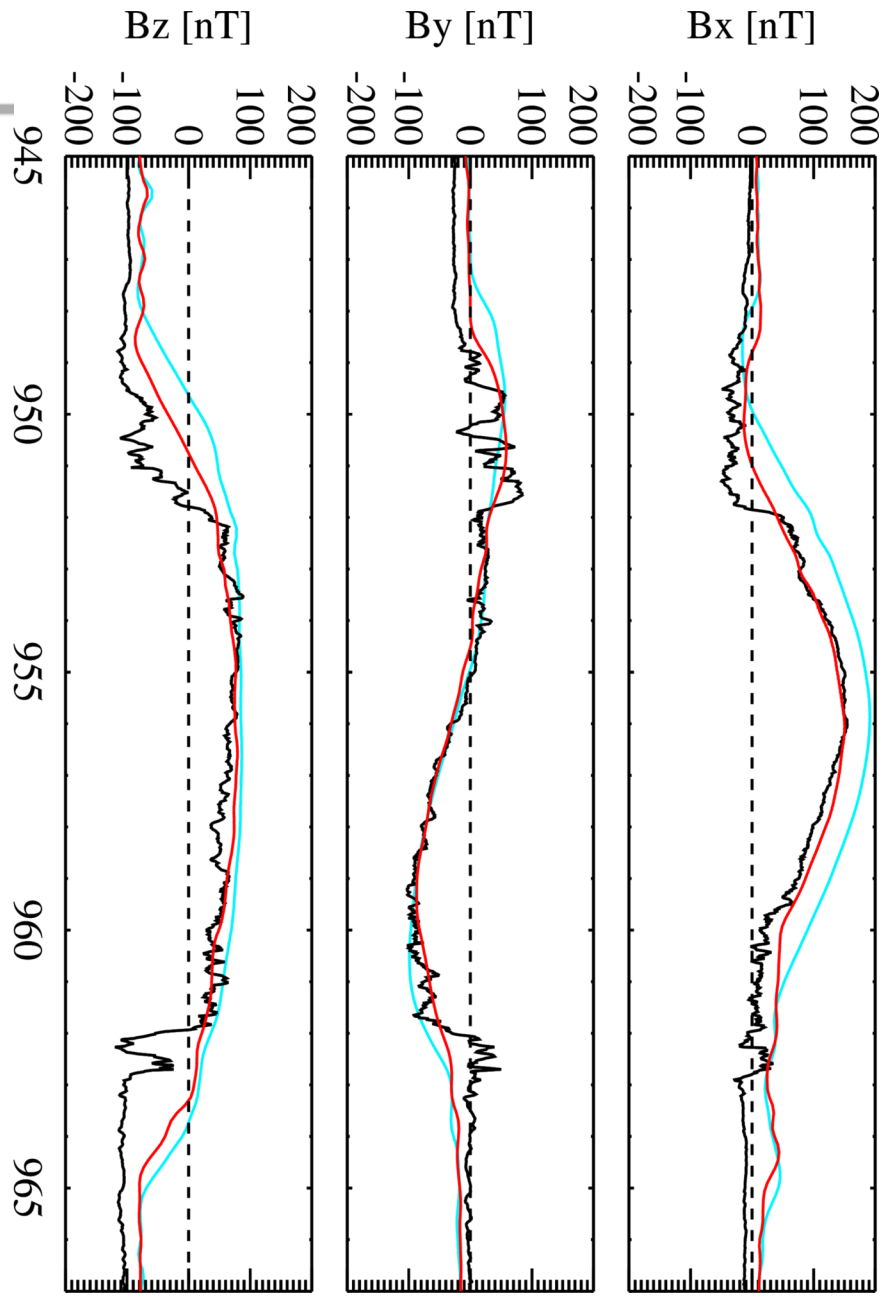
2015ja021997-f04-z-



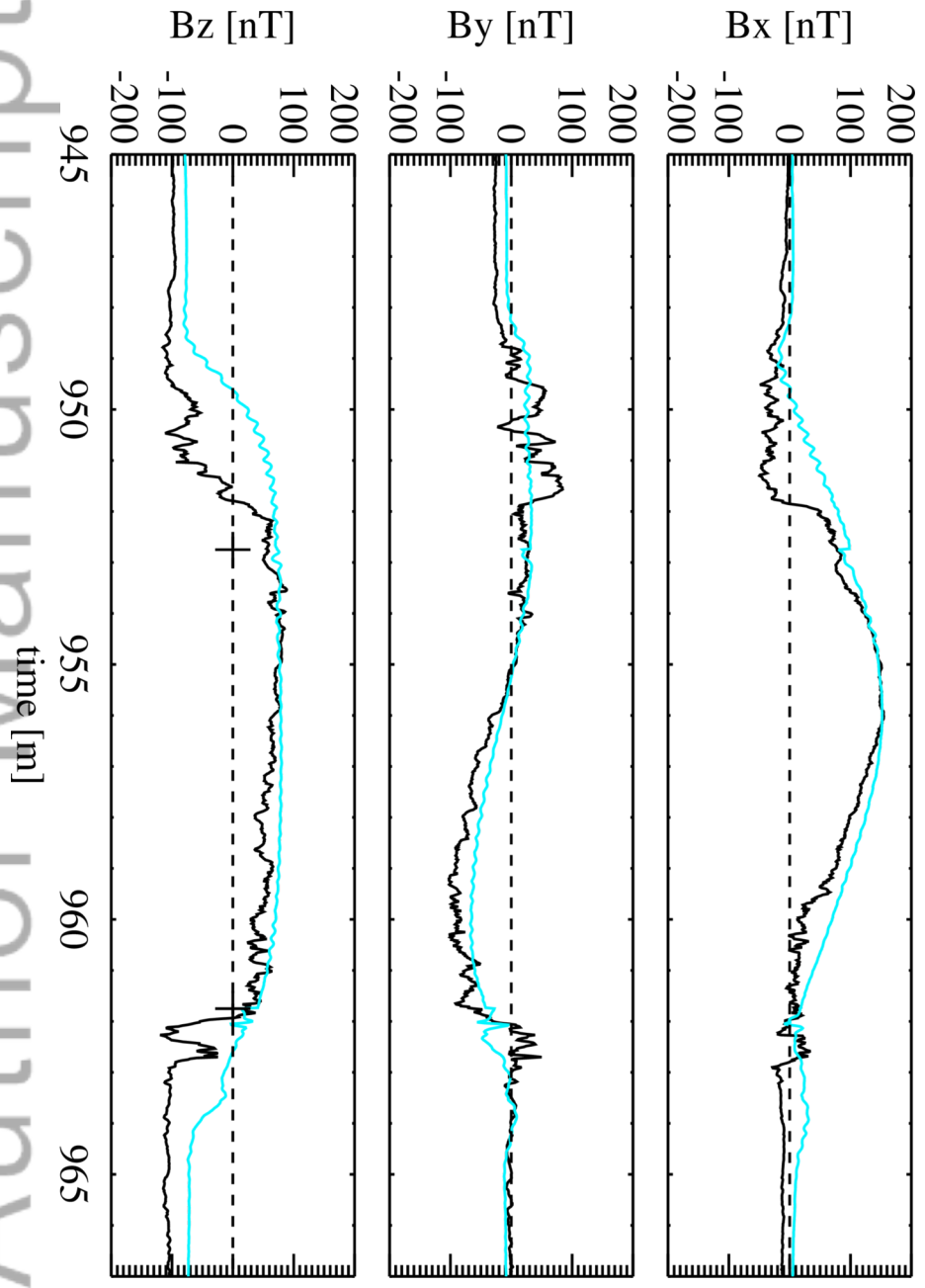
2015ja021997-f05-z-



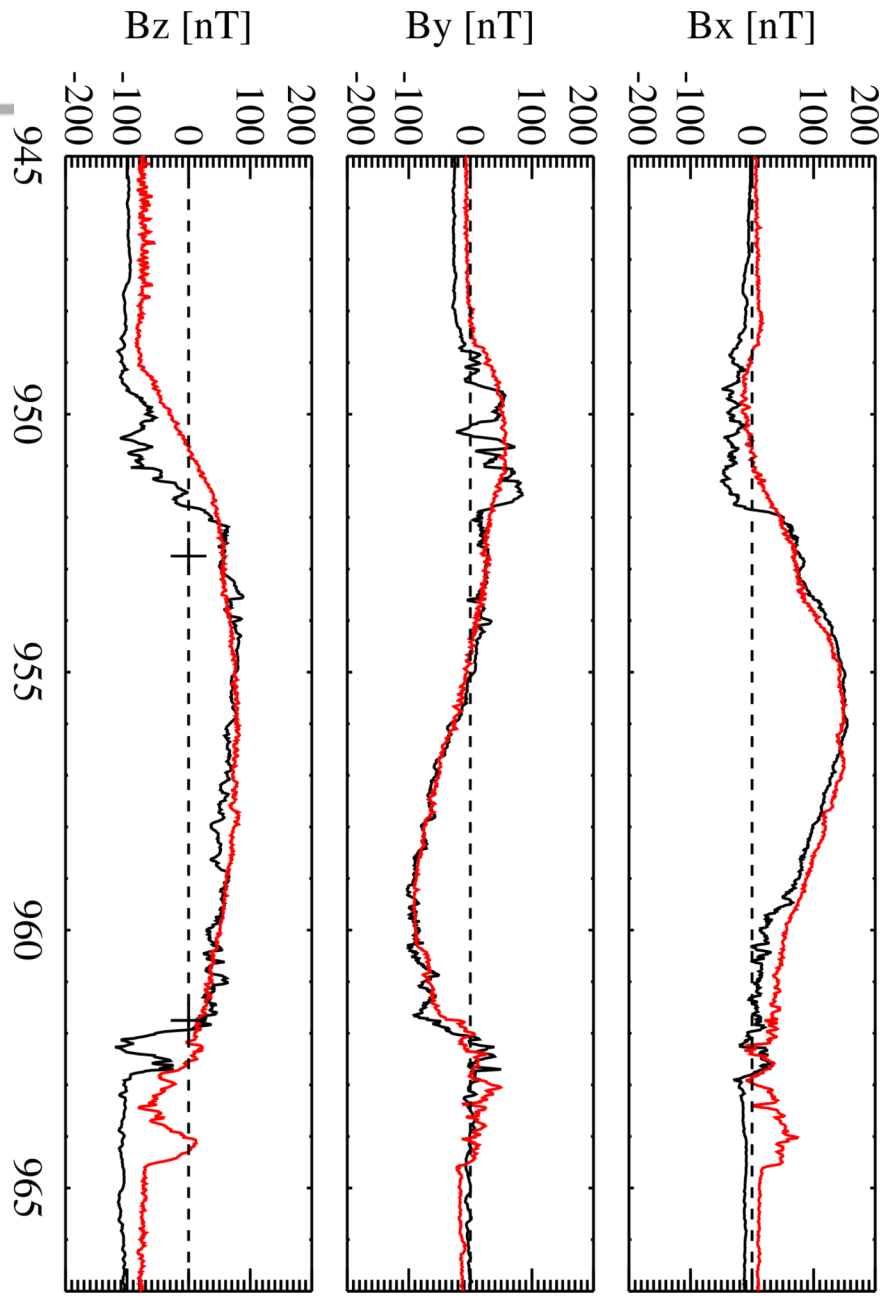
2015ja021997-f06-z-



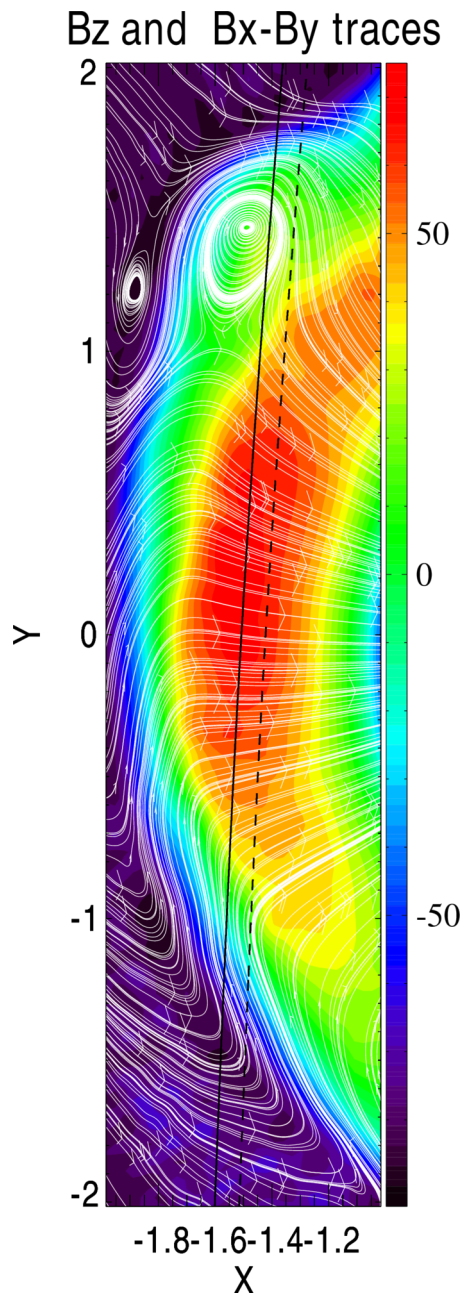
2015ja021997-f07-z-



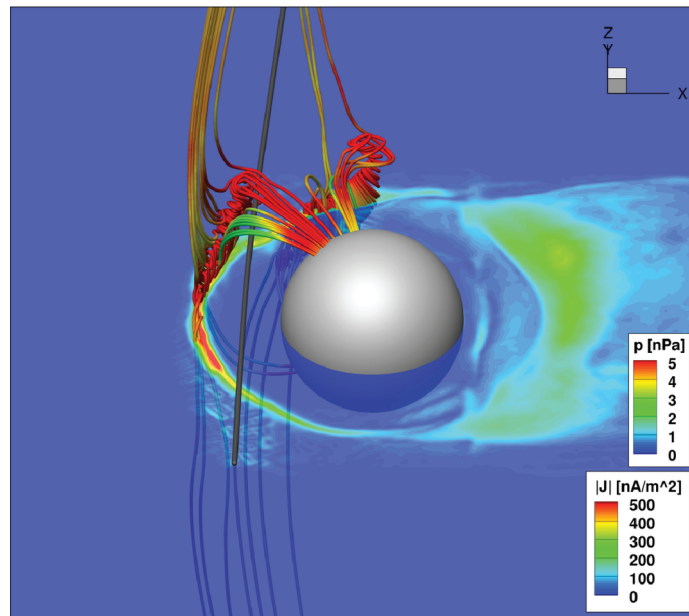
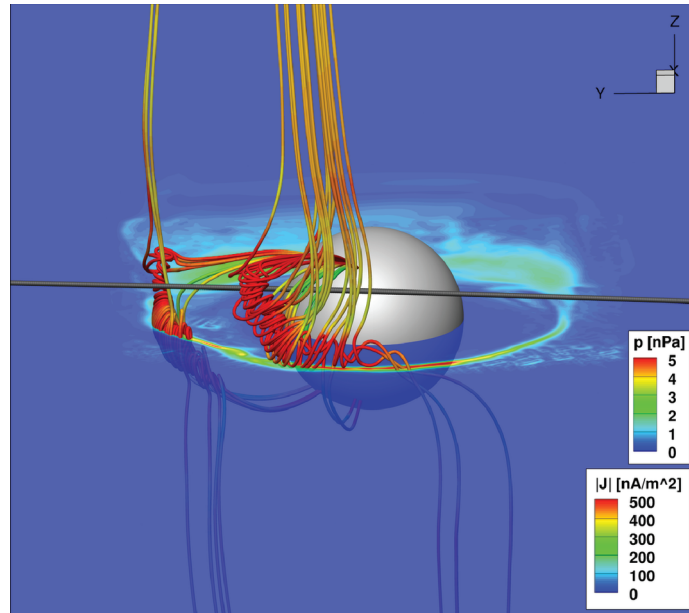
2015ja021997-f08-z-



2015ja021997-f09-z-

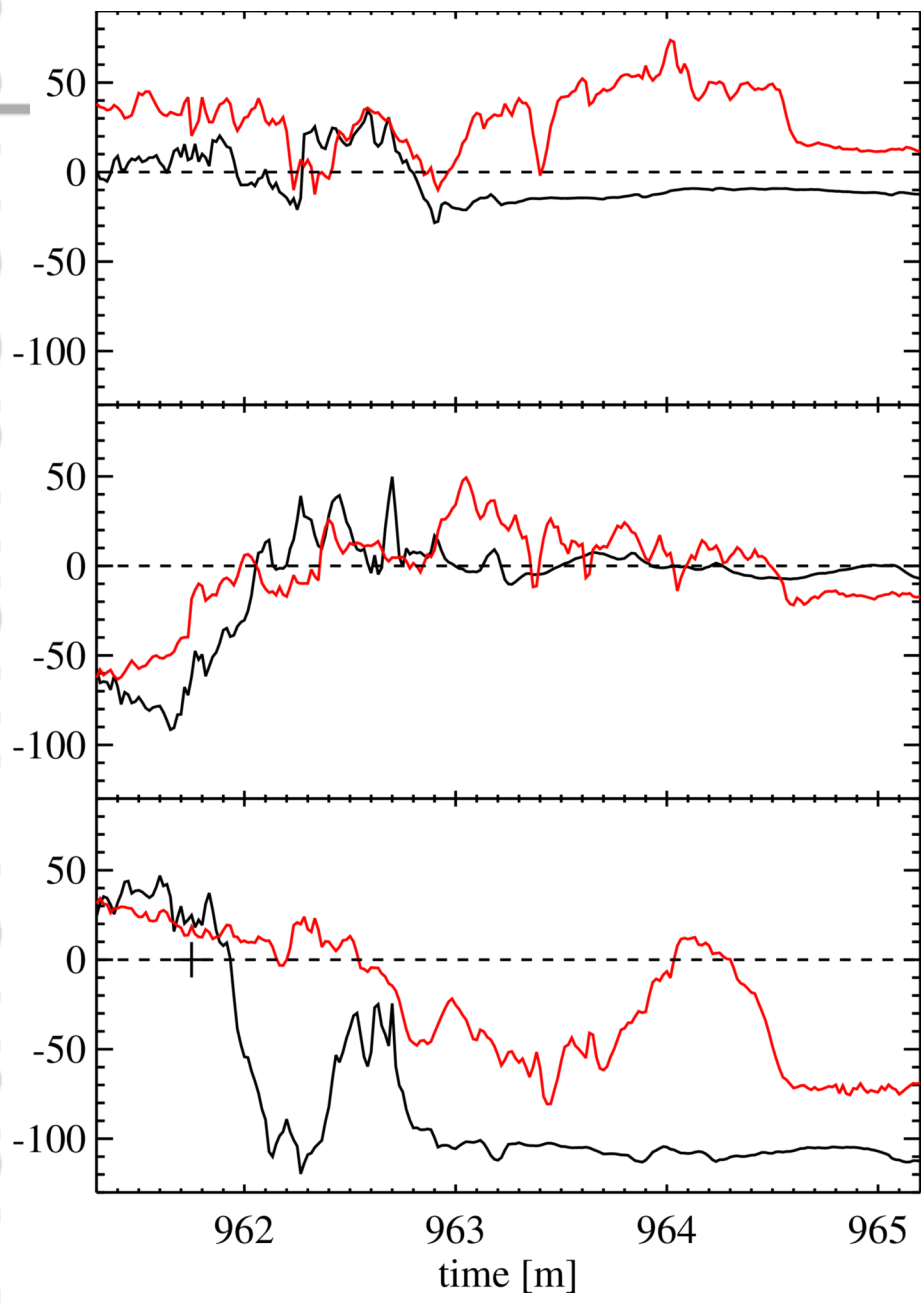


2015ja021997-f10-z-

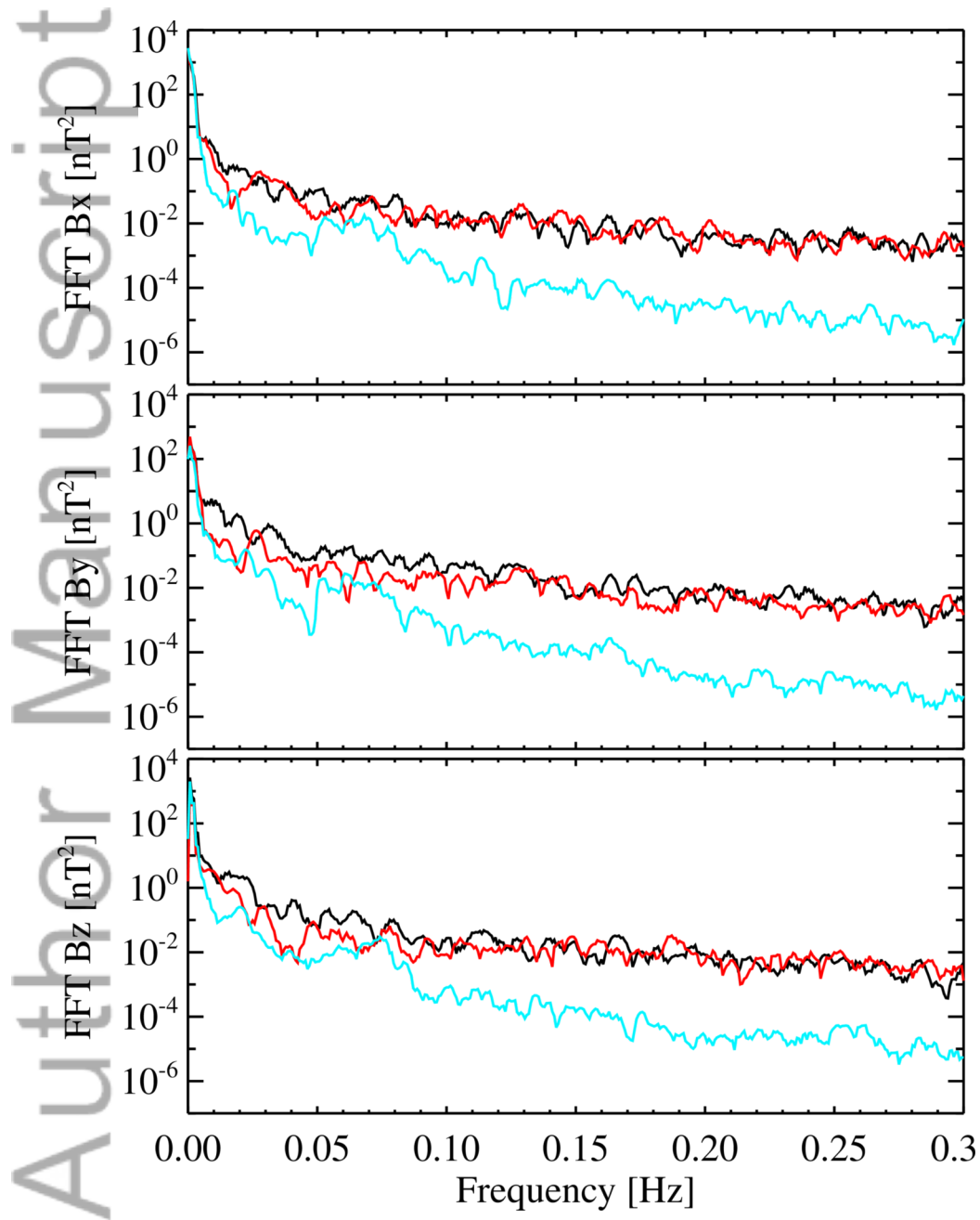


2015ja021997-f11-z-

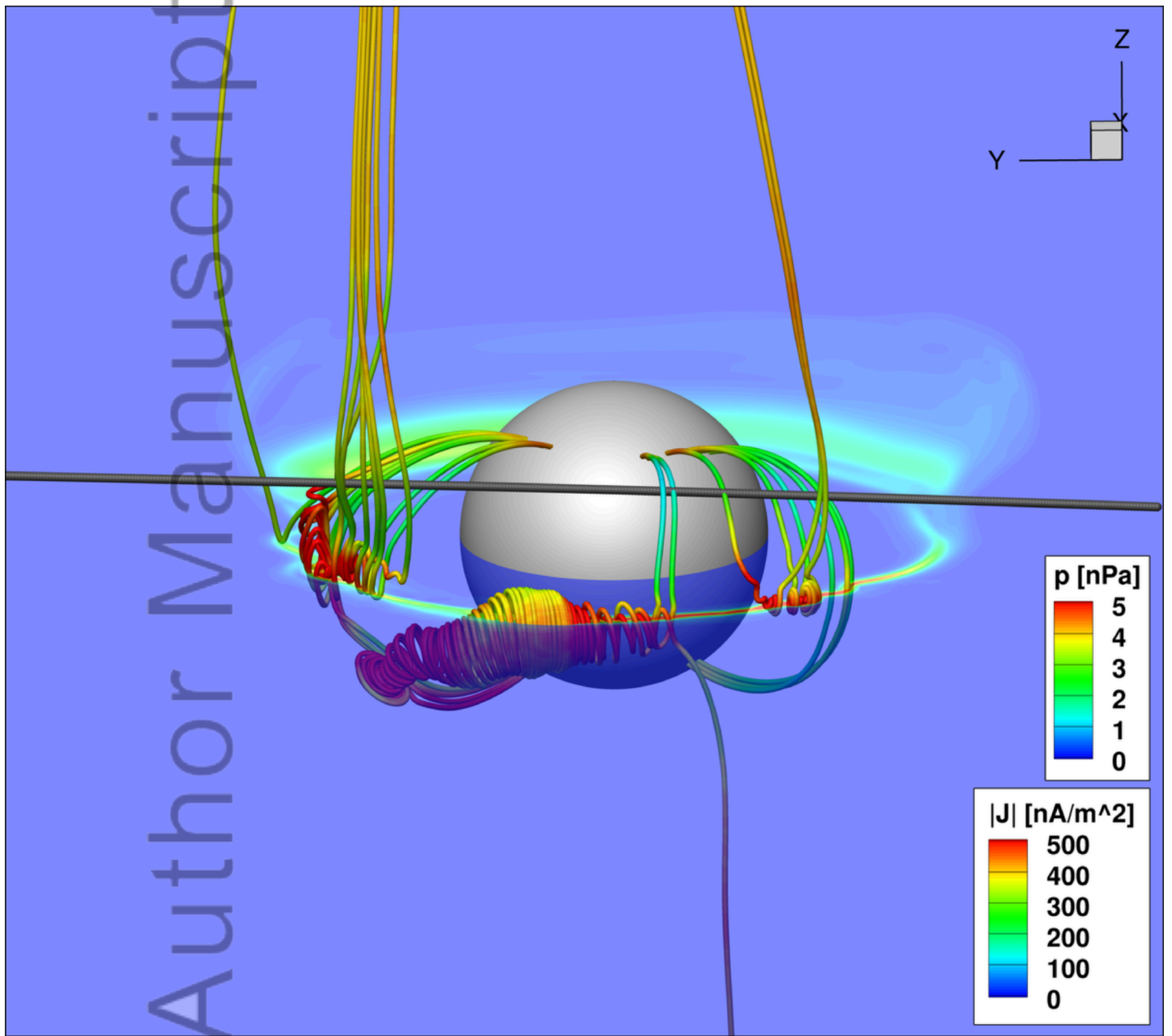




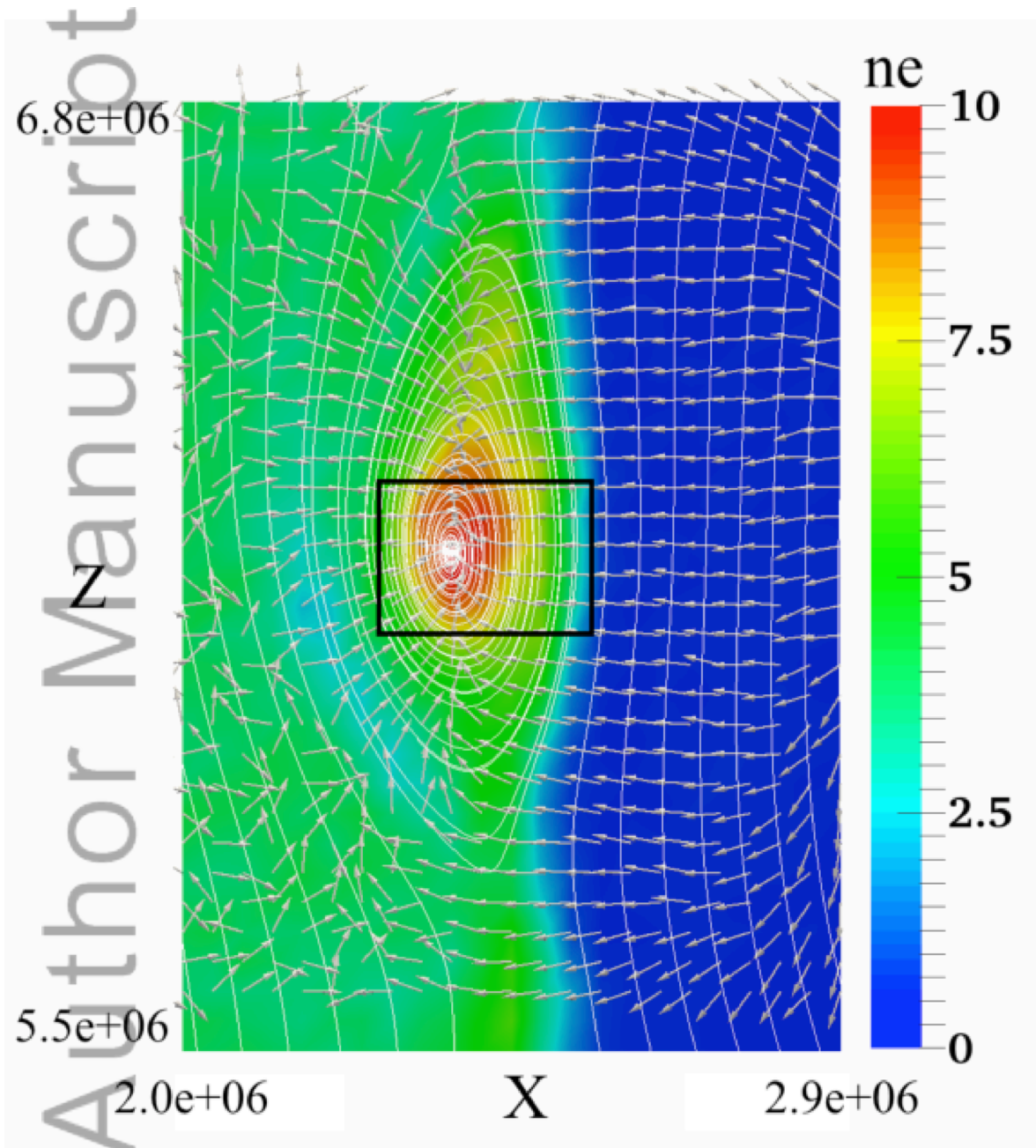
2015ja021997-f12-z-



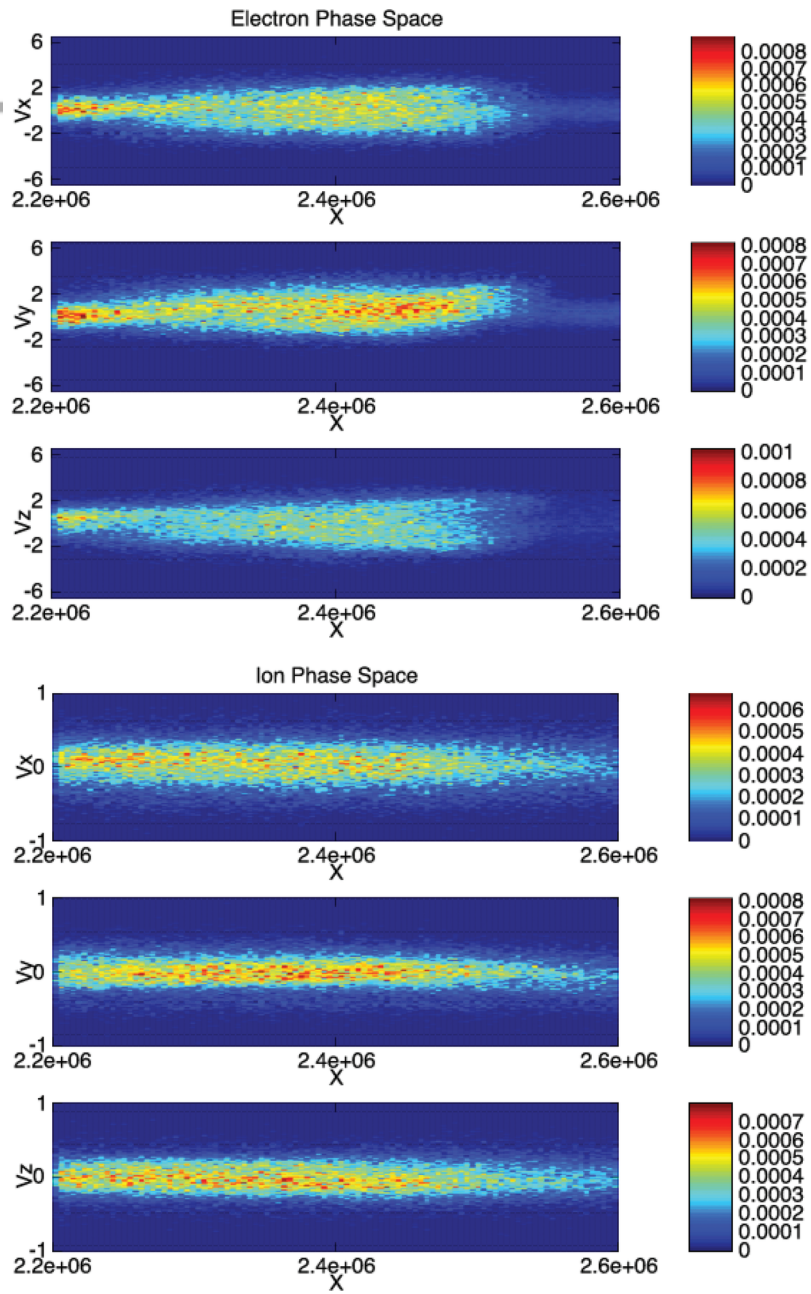
2015ja021997-f13-z-



2015ja021997-f14-z-



2015ja021997-f15-z-



2015ja021997-f16-z-

